

**A STUDY OF THE MECHANICAL BEHAVIOUR OF  
NANOCRYSTALLINE METAL FILMS**

**Proefschrift**

ter verkrijging van de graad van doctor

aan de Technische Universiteit Delft,

op gezag van de Rector Magnificus prof. dr.ir. J.T.Fokkema

voorzitter van het College voor Promoties,

in het openbaar te verdedigen op maandag 27 maart 2006 om 15:30 uur

door Nail Raufovich SHAMSUTDINOV

Engineer-physicist (Moscow Engineering-Physics Institute, State University)

geboren te Troitsk, Rusland

Dit proefschrift is goedgekeurd door de promotor:

Prof. dr. B.J. Thijsse

Toegevoegd promotor:

Dr. A.J. Böttger

Samenstelling promotiecommissie:

Rector Magnificus, voorzitter

Prof. dr. B.J. Thijsse, Technische Universiteit Delft, promotor

Dr. A.J. Böttger, Technische Universiteit Delft, toegevoegd promotor

Prof. dr. O. Thomas, Université Paul Cézanne, Marseille

Prof. dr. ir. S. van der Zwaag, Technische Universiteit Delft

Prof. dr. J.H.W. de Wit, Technische Universiteit Delft

Prof. dr. ir. E. van der Giessen, Rijksuniversiteit Groningen

Dr. ir. F.D. Tichelaar, Technische Universiteit Delft

ISBN 90-9020501-2

# CONTENTS

<b>CHAPTER I:</b>	<b>General Introduction</b>	<b>4</b>
<b>CHAPTER II:</b>	<b>A method for the experimental determination of surface photoemission core-level shifts for 3d transition metals</b>	
Introduction		11
Experimental		
A. X-ray photoelectron spectroscopy		12
B. Copper single crystals		13
Data analysis		
A. Estimation of surface contribution to photoelectron emission spectra		14
B. Analysis of photoemission spectra		15
Results and discussion		
A. Surface and bulk photoelectron emission peaks of Cu		17
B. Asymmetry and broadening of surface peaks: (111) and (100) Cu surfaces		19
C. Surface core-level shifts for (111) and (100) Cu surfaces		20
Conclusions		24
References		23
<b>CHAPTER III:</b>	<b>Grain coalescence and its effect on stress and elasticity in nanocrystalline metal films</b>	
Introduction		28
Coalescence model for films with columnar grain morphology		30
Experimental results		36
Discussion		39
Conclusions		44
References		45

<b>CHAPTER IV: Mechanical properties of and the role of dislocations and grain boundaries in nanocrystalline thin layers: the case of Fe films</b>	
Introduction	47
Methods	
A. Film deposition, morphology, crystal structure and texture	48
B. Stress evolution with temperature and Young's modulus determination	49
C. Micro-strain analysis	51
Results	54
Discussion	58
Conclusions	60
References	61
 <b>CHAPTER V: The effect of Cu interlayers on grain size and stress in sputtered Fe-Cu multilayered thin films</b>	
Introduction	64
Experimental methods	64
Results	65
Discussion	68
Conclusions	73
References	74
 <b>SUMMARY</b>	76
 <b>SAMENVATTING</b>	79
 <b>ACKNOWLEDGEMENTS</b>	82
 <b>CURRICULUM VITAE</b>	83

# CHAPTER I

## GENERAL INTRODUCTION

Miniaturization is one of the most important fields of scientific and industrial progress. Most of the research and development efforts are concerned with mastering phenomena at ever decreasing dimensions, with the cutting edge being currently at nano-scale (sub-100-nm level). The expected success of nano-materials can be illustrated by the booming research activity in the area. The use of the term 'nano' in scientific literature has grown exponentially during last decade. More than 30000 articles on 'nano' were published in 2004, which is more than twice the amount of papers on 'silicon' in the same year and nearly four times more frequent than publications on 'steel'.<sup>1</sup>

Nano-research covers a very broad field of materials science, as there are various reasons for miniaturization. Like the requirement to accommodate an as high as possible density of components in electronics: currently nodes smaller than 100 nm are produced and it is expected to nearly halve the sizes within the next 5 years.<sup>2,3</sup> In other cases, the properties, that lead to unique applications, can only be achieved at very small sizes where surface/interface properties become prominent or where small-scale phenomena such as locally intense magnetic fields can be utilized. Examples of such applications include the use of surface plasmonic properties of metallic nanostructures for photonic signal manipulation,<sup>4</sup> simultaneous ligand organization on gold nanoparticles<sup>5</sup> and, electronic and electromechanical properties of metallic nanowires.<sup>6-7</sup> Also, manufacturing issues such as reducing the amount of expensive materials drive engineers to smaller dimensions, like in the case of prospective high-temperature superconducting cables.<sup>8</sup> In this case epitaxy, texture and stability of layers as thin as few nanometers are essential for a successful commercial usage.

A material with grain size less than 100 nm at least in one dimension is generally considered as nanocrystalline material. That the physical properties of such materials are often different from their bulk counterparts may be the result of various causes, like higher

density of grain boundaries, smaller volumes of coherent crystallinity, or geometrical limitations for defects such as dislocations or stacking faults. Some of the properties different from that of bulk material are highly desired, some of them are artifacts to avoid. Understanding and controlling the size-dependent properties is the main challenge for the ongoing miniaturization.

This thesis deals with the mechanical properties and structure of nanocrystalline metal films. The same general properties of metals that make them so widely used as coarse-grained materials are very promising at nano-scale as well. In particular the mechanical behavior of nanocrystalline metals is interesting as it differs from that of bulk material and directly affects the stability of components. During last decades a considerable effort has been made in understanding mechanical behavior of nanocrystalline metals. A wealth of experimental and computational data is now available. The (few) key observations that characterize the mechanical properties of nanocrystalline metals will be outlined next.

It was recognized long time ago that plasticity of metals depends on grain size. Due to dislocation pile-up at grain boundaries, the yield strength  $\sigma_y$  of coarse-grained material increases with decrease of grain size  $d$  following the Hall-Petch behavior,<sup>9,10</sup>

$$\sigma_y = \sigma_0 + kd^n, \quad (1)$$

where  $n = -1/2$ ,  $\sigma_0$  and  $k$  are constants. For nanocrystalline metals, however, it is established that the Hall-Petch relation (1) with classical exponent of  $-1/2$  does not hold. Fig. 1 shows the experimental data for copper, discussed in Ref. 11, with evident deviations from the classical exponent. Moreover, at grain sizes below 10 nm a softening is frequently observed.

These deviations in plasticity of nanocrystalline metals became the focus of an extensive research effort during past decade. Computations suggest that the role of grain boundaries can be paramount: they are able to affect stress states through grain boundary sliding (GBS) and, can absorb and emit dislocations (see Ref. 12 for overview). However, there is a lack of experimental data to validate the existing computational models. Accurate experimental analysis is challenging because of the difficulties associated with the precise determination of the role of the morphology of nanocrystalline metals. The impact of such parameters as grain size and shape, texture and density on mechanical properties needs to be addressed more explicitly.

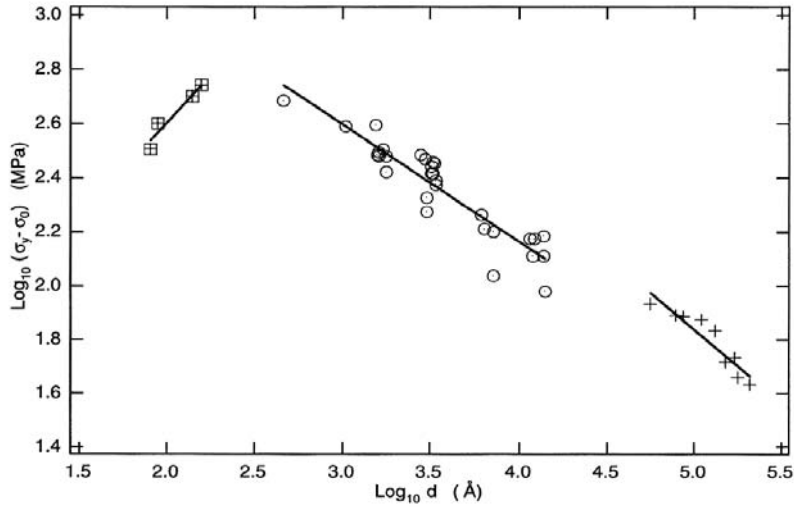


Fig. 1. Experimental data on yield strength as a function of grain size  $d$  of nanocrystalline copper and Ag/Cu multilayers from Ref. 11. The fitted exponent  $n$  varies from  $-0.43$  to  $+0.93$ .

Nanocrystalline metals exhibit anomalous elasticity, in the sense that the elastic modulus is usually lower than the bulk value.<sup>11,13,14</sup> Despite the importance of this phenomenon for understanding the mechanical behavior of nanocrystalline metals, this issue attracted relatively little attention as compared to anomalous plasticity. Existing explanations of the elastic anomaly in nanocrystalline metals include the GBS mechanism, the influence of micro-cracking and the anomalous properties of the so-called ‘grain boundary phase’.

The GBS mechanism is based on the assumption of the inability of grain boundaries to sustain strong shear stresses.<sup>15</sup> As a result, the stress under an external *uniaxial* straining redistributes in such a way that the Young modulus of a film is effectively reduced. But for a *biaxial* stress state the GBS model predicts too little or no reduction of Young’s modulus, although considerable reduction in modulus is observed in experiments with biaxial symmetry as well.<sup>14</sup> The micro-cracking mechanism requires considerable grain boundary damage to be present in the material.<sup>11</sup> As a result of this damage, the stress cannot be fully transferred through material. The third mechanism suggested in literature, i.e. enhanced grain boundary compliance,<sup>13</sup> considers grain boundaries as a second phase with different properties. As a result of this division in two separate phases, this model’s predictions depend on the grain boundary thickness and elastic properties of the grain boundary phase, which are both not measurable parameters and rather arbitrarily assigned. Furthermore, despite an extensive experimental effort, there are no indications that such grain boundary phase is

present in nanocrystalline metals (see discussion in Ref. 12). At the moment, there is no common agreement about the dominant mechanism that governs anomalous elastic response of nanocrystalline metals.

As the grain size in a material decreases, the density of surfaces, grain boundaries, and interfaces rises, and their role becomes prominent. For a quantitative description of phenomena in nanocrystalline material it is important to know the surface/interface characteristics such as surface, interface/adhesion energies. However, there are no direct experimental methods to measure these parameters for crystalline materials. The surface energies, for example, are often determined using extrapolations from melting temperatures,<sup>16</sup> or calculated using *ab initio* approaches.<sup>17</sup> The accuracy of the extrapolations is limited and to establish the predictive capability of calculations experimental results are required. It is therefore important to explore experimental methods that can help to gather thermo-chemical data of surfaces and interfaces of crystalline metals.

In the present thesis the emphasis is on the investigation of the 3d transition metals, as this group represents industrially important elements, such as iron and copper. The size-dependent mechanical properties have been studied on the example of these metals. Interface and surface phenomena, specific for these metals, also are addressed.

One of the possible experimental approaches to determine surface properties of a metal is by X-ray core-level photoelectron spectroscopy (XPS).<sup>18</sup> The high surface sensitiveness of XPS (the penetration depth of electrons in metals is typically within a few nanometers) results in significant surface contribution to the measured spectra. During past two decades it was demonstrated on the example of 4d and 5d transition metals that core-level photoelectron spectroscopy quite accurately measures surface segregation energies (see Ref. 19 for overview).

However, application of the method to the 3d transition series was hindered because of the large photoelectron line width of these metals. As a consequence, the overlapping surface and bulk contributions are very difficult to resolve. In Chapter II an experimental approach is presented that overcomes this difficulty.

In Chapter III a combined experimental and theoretical study is presented that employs a grain coalescence model to describe the anomalous elastic behavior and the occurrence of tensile stress in nanocrystalline materials. The experimental part of the study



on magnetron sputtered nanocrystalline Fe thin films demonstrated a good agreement of the model predictions for both stress and elasticity.

Thin metal films and multilayers attract tremendous academic attention due to a number of prospective applications. In the remaining two chapters the results of experimental investigations of mechanical behavior of nanocrystalline iron thin films (Chapter IV) and Fe/Cu multilayers (Chapter V) are presented. Both studies focus on the development of stress states upon annealing and an analysis of the relationship between morphological characteristics and mechanics. In Chapter IV the experimental analysis of the thermal response of mechanical parameters such as stress, elastic modulus, and certain aspects of dislocations' behavior is presented for the case of nanocrystalline Fe thin films. Also a description of the method, developed to estimate geometrical characteristics of dislocations in bcc metals, namely distribution of dislocations by orientation of their Burgers vector is given.

Nanocrystalline metallic multilayers offer vast opportunities in tailoring various material properties. For example, combining immiscible iron and copper, one can easily control the grain size in sputtered material, as demonstrated in Chapter V in the experimental study of Fe/Cu multilayers.

## REFERENCES

- 1 D.J. Eaglesham, MRS Bulletin **30**, 260 (2005).
- 2 International Technology Roadmap for Semiconductors, 2004 Update, Interconnect; <http://public.itrs.net/>
- 3 MRS Bulletin **29**, No. 11, 805-851 (2005).
- 4 MRS Bulletin **30**, No. 5, 338-389 (2005).
- 5 P.V. Braun, Nature Materials **3**, 281 (2004).
- 6 B. Wu, A. Heidelberg, and J.J. Boland, Nature Materials **4**, 525 (2005).

- 7 L. Mohaddes-Ardabili, H. Zheng, S.B. Ogale, B. Hannoyer, W. Tian, J. Wang, S.E. Lofland, S.R. Shinde, T. Zhao, Y. Jia, L. Salamanca-Riba, D.G. Schlom, M. Wuttig, and R. Ramesh, *Nature Materials* **3**, 533 (2004).
- 8 MRS Bulletin **29**, No. 8, 533-589 (2004).
- 9 N.J. Petch, *J. Iron Steel Inst.* **174**, 25 (1953).
- 10 J.C.M. Li, and Y.T. Chou, *Met. Trans.* **1**, 1145 (1970).
- 11 H. Huang, and F. Spaepen, *Acta Mater.* **48**, 3261 (2000).
- 12 K.S. Kumar, H. Van Swygenhoven, and S. Suresh, *Acta Mater.* **51**, 5743 (2003).
- 13 P. Sharma, and S. Ganti, *J Mater Res* **18**, 1823 (2003).
- 14 M.M. De Lima Jr., R.G. Lacerda, J. Vilcarromero, and F.C. Marques, *J Appl. Phys.* **86**, 4936 (1999).
- 15 C. Zener, *Phys. Rev.* **60**, 906 (1941).
- 16 F.R. de Boer, R. Boom, W.C.M. Mattens, A.R. Miedema and A.K. Niessen, *Cohesion in Metals* (Elsevier Science Publishers, Amsterdam, 1988), Vol. 1.
- 17 A. Christensen, A.V. Ruban, P. Stoltze, K.W. Jacobsen, H.L. Skriver, J.K. Nørskov and F. Besenbacher, *Phys. Rev. B* **56**, 5822 (1997).
- 18 B. Johansson, and N. Martensson, *Phys. Rev. B* **21**, 4427 (1980).
- 19 M. Aldén, I.A. Abrikosov, B. Johansson, N.M Rosengaard, and H.L Skriver, *Phys. Rev. B* **50**, 5131 (1994).
- 20 W.D. Nix, and B.M. Clemens, *J Mater. Res.* **14**, 3467 (1999).

## CHAPTER II

# **A METHOD FOR THE EXPERIMENTAL DETERMINATION OF SURFACE PHOTOEMISSION CORE-LEVEL SHIFTS FOR 3d TRANSITION METALS**

N.R. Shamsutdinov, W.G. Sloof and A.J. Böttger

*Department of Materials Science and Engineering, Delft University of Technology,  
Rotterdamseweg 137, 2628 AL Delft, The Netherlands*

### ABSTRACT

A method is presented to determine photoelectron surface core-level shift (SCLS) of 3d transition metals using X-ray photoelectron spectroscopy (XPS). The experimental difficulties arising from the relatively large broadening of photoemission lines in the 3d transition series can be overcome by analysis of the angular dependence of photoemission spectra. The proposed method has been demonstrated using well-defined single crystal surfaces of copper. The observed values of the SCLS for copper are compared with those predicted by both *ab initio* calculations and a macroscopic atom model. The experimental determination of surface core-level shifts (SCLS) opens alternative routes for collecting thermo-chemical data for surfaces/interfaces.

## I. INTRODUCTION

During the past two decades considerable progress has been achieved in understanding the physics of core-level photoemission from surface atoms of pure metals. It is now firmly established that atoms at a metallic surface yield a photoelectron response different from that in the bulk, i.e. shifted peak position, different singularity index, lifetime and phonon broadening. Theoretical and experimental studies of broadening and asymmetry of the surface peak have mainly focused on W,<sup>1</sup> Ta<sup>2,3</sup> and alkali metals (Ref. 4 and references therein), demonstrating a higher singularity index and broadening for photoelectron emission from surface atoms. A lot of attention has been paid to the investigation of the shift of the surface peak position with respect to the bulk peak position (see Ref. 5 for a review) because it could be used to obtain thermo-chemical data of the surface, such as the surface and segregation energies. Johansson and Martensson<sup>6</sup> demonstrated that the main contribution to the core-level shifts of a metal with atomic number  $Z$  is the cohesive energy difference between metal  $Z+1$  and  $Z$ . This implies that the difference between the surface and the bulk photoelectron peak positions is related to the segregation energy of metal  $Z+1$  as an impurity to the surface of metal  $Z$ .<sup>7</sup> Surface energies, segregation energies and related properties such as work of adhesion are of importance for the rapidly developing field of surface and interface engineering. Since no methods for precise and direct experimental measurement of surface and segregation energies of crystalline materials are currently available, the measurement of photoelectron shifts is potentially a powerful tool for the collection of thermo-chemical data for metallic surfaces that otherwise only could be obtained theoretically using both *ab initio*<sup>5</sup> and semi-empirical<sup>8</sup> models. Extensive experimental and numerical studies of surface core-level shifts (SCLS) were carried out for many pure metals, especially from the 4d and 5d transition series (see Ref. 5 and references therein). The experimental attempts to determine SCLSs in 3d metals are very few and inconclusive.<sup>9,10</sup> This is due to the relatively complex photoelectron spectrum of these metals, i.e. the large intrinsic peak widths (of the order of the expected shift or more) that hinders unambiguous peak separation when resolving these spectra by curve fitting.

In this chapter a method is presented for determination of the SCLS of 3d transition metals from measured photoelectron spectra. One of the earliest works on SCLSs (Ref. 9) demonstrated a method for determination of SCLSs (for polycrystalline evaporated Cu films)

from photoelectron spectra recorded at several observation angles. The underlying idea is that the observation angle determines the analysis depth of the photoelectrons, and thus spectra, with different surface contributions, recorded by varying the observation angle. By analyzing the spectra simultaneously, the surface and the bulk contributions can be distinguished. The work ignores the substantial differences in singularity indices and broadening for bulk and surface peaks. By taking into account today's knowledge of core-level photoemission from metallic surfaces, the method can be improved significantly. In addition it will be shown that the condition of the surface, i.e. roughness, crystallographic orientation, imperfections etc. can have major influence on the results.

The method is demonstrated here using X-ray photoelectron emission spectra recorded from clean, crystallographically perfect, single crystal copper surfaces. Three differently oriented copper surfaces were investigated: (111), (100) and (110). The values for the SCLSs obtained from these XPS measurements are compared with those determined using a semi-empirical "macroscopic atom" model and with *ab initio* calculations.

## II. EXPERIMENTAL

### A. X-ray photoelectron spectroscopy

The XPS analysis was performed with a PHI 5400 ESCA system equipped with a dual anode X-ray source (Mg/Al) and a spherical capacitor analyzer (SCA). The X-ray source was operated at 15 kV and 400 W generating a non-monochromatic incident Mg X-ray radiation (Mg  $K\alpha_{1,2}$  = 1253.6 eV). The energy scale of the SCA was calibrated according to a procedure described in Ref. 11. The instrument was set at a constant analyzer pass energy of 35.75 eV when measuring the C  $1s$  and the O  $1s$  photoelectron lines and at 8.95 eV when measuring the Cu  $2p$  and Cu  $3s$  photoelectron lines. The spectra from the C  $1s$  and O  $1s$  photoelectron lines were recorded with a step size of 0.2 eV and those of the Cu  $2p$  and  $3s$  photoelectron lines with a step size of 0.1 eV. The electrons emitted from the sample were detected at angles  $\theta$  of 20°, 30°, 45° and 60° (with respect to the sample surface). The elliptic analysis area of the sample surface is given by  $1.1 \times 1.1 / \sin \theta$  mm.

Although the application of non-monochromatic Mg  $K\alpha$  radiation increases the instrumental broadening (as compared to a monochromated source), the overall peak shape is well described<sup>12</sup> by means of the Doniach-Sunjić (DS) peak form.<sup>13</sup> It has been proved that

such a peak form is a physically justified model for profile analysis of the photoelectron spectra of pure metals. The Cu  $2p_{3/2}$  photoelectron emission line investigated in this work was chosen because it is fully separated from the Cu  $2p_{1/2}$  and is less broadened than the  $3s$  emission line. The surface sensitivity (the intensity ratio between surface and bulk contributions) when using Mg  $K_{\alpha}$  radiation is also higher for photoelectrons emitted from the  $2p$  than from the  $3s$  shell.

## **B. Copper single crystals**

Three different copper single crystal surfaces were studied: Cu (100), (110) and (111). These Cu single crystals with a purity of 5N were prepared using the Czochralski method (Surface Preparation Laboratory, Zaandam, the Netherlands). The single crystal samples, with a diameter of 10 mm and thickness of 2 mm, were polished on one side with 50 nm oxide particle suspension in the final step. The orientation of the crystal surfaces was verified using the Laue method and was within  $0.5^{\circ}$ .

Copper was chosen because the value expected for the SCLS is relatively large (see estimates given in Section IV.C). In addition, the copper surfaces studied do not exhibit surface reconstruction<sup>14</sup> and the surface of copper can be cleaned and recovered in UHV.

Prior to the XPS measurements the Cu single crystal surfaces were sputter-cleaned (with 1 keV  $\text{Ar}^{+}$  for 15-30 min) and then annealed for 5 min at 800 K in an UHV chamber directly coupled to the XPS equipment (base pressure  $\leq 1 \cdot 10^{-7}$  Pa). This procedure was repeated twice. The annealing treatment is necessary to recover the Cu surface, which becomes damaged by the sputter-cleaning process. The level of oxygen and carbon contamination was monitored during the XPS measurements by recording their  $1s$  photoelectron lines: the oxygen and carbon levels were below the detection limit of about 0.01 monolayer. After the XPS measurement the orientation and the quality of the Cu single crystal were verified with a Scanning Electron Microscope (Jeol JSM 6500F) by means of Electron Back-Scattering Diffraction (HKL Technology). The results indicate that the surface crystallinity after annealing has been restored fully.

### III. DATA ANALYSIS

#### A. Estimation of surface contribution to photoelectron emission spectra

The take-off or observation angles  $\theta$  (measured with respect to the sample surface) were chosen such that a sufficient change in the relative contributions of the surface and bulk intensity is achieved. Estimates of these relative contributions can be made with a simple approximation by considering the surface layer as just the upper monolayer of atoms. The layer directly below the surface is considered as bulk i.e. all the atoms are considered as fully surrounded by nearest neighbors. First, the (111) and (100) surfaces are considered, leaving the case of the (110) surface for later discussion. If  $d$  is the thickness of a surface layer and  $\lambda$  is the electron inelastic mean free path (IMFP), then the photoelectron intensity ratio  $k$  of surface to bulk contribution is given by:

$$k = \frac{I_{surf}}{I_{bulk}} = \int_0^d e^{-z/\lambda \sin \theta} dz \bigg/ \int_d^\infty e^{-z/\lambda \sin \theta} dz = e^{d/\lambda \sin \theta} - 1 \quad (1)$$

A considerable change in the relative contribution of the surface layer intensity to the Cu  $2p_{3/2}$  peak is expected within the take-off angle range of  $20^\circ$  to  $60^\circ$  for Mg  $K_\alpha$  radiation (see Table I). In these calculations, the effect of photoelectron diffraction (which may cause variations of up to 75% of the maximum intensity<sup>16</sup>) has been ignored. Thus Eq. (1) cannot be used to calculate the precise intensity ratios for the surface of a single crystal. In this work Eq. (1) is only used to consider the trend between the surface to bulk intensity ratio and the photoelectron take-off angle.

TABLE I. Surface to bulk intensity ratio  $k$  according to Eq. (1) for the Cu  $2p_{3/2}$  photoelectron line of Cu (100) and Cu (111) single crystal surfaces at different take-off angles  $\theta$  ( $\lambda=0.785$  nm taken from Ref. 15).

$\theta$ ( $^\circ$ )	$k_{(100)}$	$k_{(111)}$
20	0.80	0.97
30	0.50	0.59
45	0.33	0.39
60	0.26	0.31

The nearest neighbors approximation allows separation of the upper surface layer (some of the nearest neighbors are missing) from the bulk atoms (all the nearest neighbors are present). For a (111) and (100) surface, the atoms in the surface layer miss 3 and 4 nearest neighbors respectively. In case of a (110) surface the atomic arrangement is more complex. Besides an upper surface layer, where the atoms miss 5 nearest neighbors, a subsurface layer (immediately below the surface layer) can also be identified where the atoms miss 1 nearest neighbor. The latter implies that a two-peak description of the photoemission line from the (110) surface is too simple, since the contribution of the subsurface layer is not included (see discussion in Ref. 3).

## B. Analysis of photoemission spectra

As a first step in the analysis of the photoelectron spectra the satellites due to the non-monochromatic nature of the X-ray source were removed. Then the contribution to the background of the photoelectron spectrum of electrons that suffered extrinsic energy losses was computed by adopting the universal Tougaard-profile.<sup>17</sup> After subtraction of this background profile an extrinsic energy-loss contribution still remains, as is evident from Fig. 1. The intensity of the background tail of the peak rises with an increasing value of the binding energy, while the intrinsic losses as described by Doniach and Sunjic (see below) are expected to steadily decrease with increasing binding energy. Thus, in addition to the universal Tougaard background profile, it is necessary to include an extra extrinsic energy loss component in the profile fitting that depends on the photoelectron emission take-off angle. This extra component is approximated by a linear function near the position of the peak maximum.<sup>18</sup>

In the profile analysis of the photoelectron spectra a Doniach-Sunjic (DS) peak shape was used:<sup>13</sup>

$$I(E) \propto \frac{\Gamma(1-\alpha)}{[(E-E_0)^2 + \gamma^2]^{(1-\alpha)/2}} \cos \left[ \frac{\pi\alpha}{2} + (1-\alpha) \tan^{-1} \left( \frac{E-E_0}{\gamma} \right) \right], \quad (2)$$

where  $I(E)$  is the photoelectron intensity as a function of the binding energy  $E$ ,  $\alpha$  is the singularity index or asymmetry parameter,  $\gamma$  is the life-time broadening and  $E_0$  – the peak maximum in the absence of lifetime broadening. The last mentioned parameter does not represent the position of the symmetric part of a peak (see Ref. 13 for details), thus, for the



analysis of the surface core-level shifts, the broadened DS-peak maximum is taken as the peak position, i.e.:

$$E_{\max} = E_0 - \gamma \cot\left(\frac{\pi}{2-\alpha}\right) \quad (3)$$

The singularity index  $\alpha$  reflects the nature of the screening charge and varies between 0 (i.e. the DS-peak shape becomes Lorentzian) and its maximum allowed value of 0.5 (see Section IV.B for details).

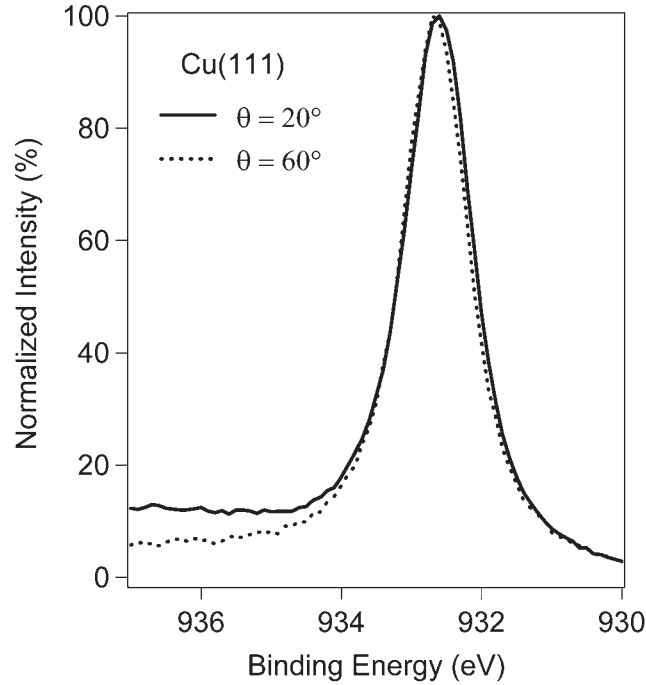


Fig. 1. Cu  $2p_{3/2}$  photoelectron spectra recorded from a Cu (111) single crystal surface at two different take-off angles  $\theta$ , showing an increase of the extrinsic losses as well as a slight but significant shift of the spectrum to lower binding energy at a grazing angle.

The surface and bulk contributions are difficult to resolve from the measured photoelectron spectra due to the large intrinsic peak width for 3d transition metals. The peak width is larger than the surface shift and therefore surface and bulk contributions merge into one broad peak. The different asymmetry of the surface and bulk photoelectron peaks adds to the complexity of the problem. Any unconstrained fitting of a single 3d-metal photoelectron spectrum with two peaks is likely to end up with physically meaningless values for the peak positions, intensities, etc. This can be overcome by considering a series of spectra recorded with different surface sensitiveness. Previously, Citrin and Wertheim<sup>9</sup> applied *simultaneous*

fitting of several spectra observed at different take-off angles with some of the parameters constrained. In that work, the asymmetry and broadening of the surface peak were forced to be equal to the bulk values, while the intensities and positions were allowed to change. However, it has been shown<sup>1-4</sup> that the surface peaks of metals have significantly different asymmetry and broadening than the bulk ones.

Therefore, the photoelectron spectra recorded at four different take-off angles (after subtraction of satellites and background signal, see above) were analyzed simultaneously by least-square fitting of the surface and bulk peaks. When fitting these two peaks, the parameters of the surface peak (i.e. intensity, position, broadening and singularity index) were set independent of their counterparts of the bulk peak. However, the position, broadening and asymmetry of the bulk peak, as well as these for the surface peak, were kept the same for all the take-off angles. The surface to bulk intensity ratios were obtained by integrating the fitted peaks with a DS-shape over the binding energy range (930 - 938 eV). The range is selected to cut off the non-linear extrinsic background contribution.

## IV. RESULTS AND DISCUSSION

### A. Surface and bulk photoelectron emission peaks of Cu

The photoelectron emission spectra of clean and recovered Cu (100), (110) and (111) single crystal surfaces and one sputter-damaged Cu (111) surface were analyzed as described in Section III. The surface and bulk peaks of a Cu (100) surface as obtained by simultaneous fitting of photoelectron emission spectra recorded at four different take-off angles are shown in Fig. 2. In Table II the values are given for the surface to bulk intensity ratio as determined from the surface and bulk peaks resolved from the measured photoelectron spectra. These values decrease with increasing photoelectron take-off angle  $\theta$  for both the Cu (100) and (111) recovered surfaces. However, such a trend is not observed for the surface to bulk intensity ratio for the Cu (110) recovered and the Cu (111) sputter-clean surfaces. These findings indicate that the applied model (i.e. a single surface layer on top of the bulk material) is not appropriate for the Cu (110) recovered and the Cu (111) sputter-clean surfaces.

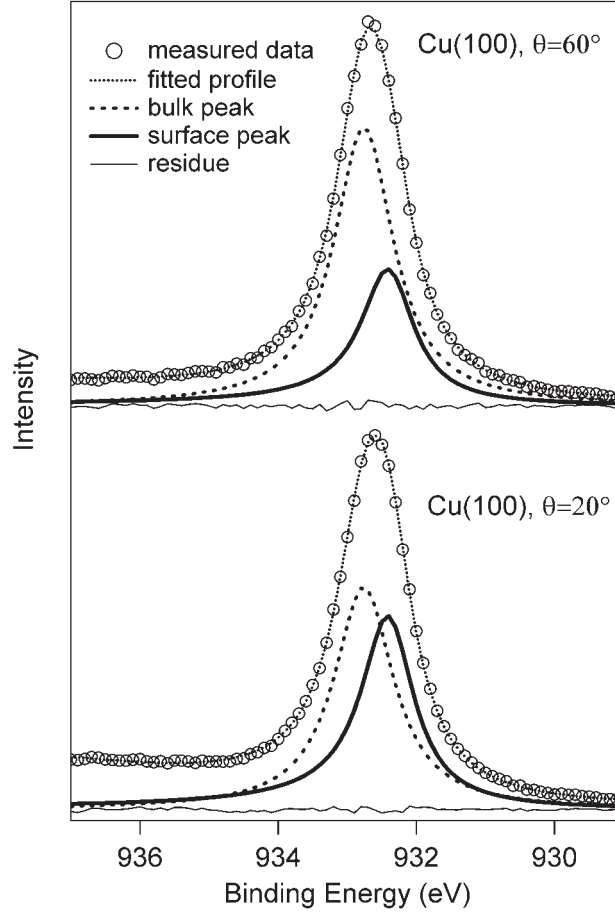


Fig. 2. Cu  $2p_{3/2}$  photoelectron spectra (after Tougaard-background and satellite subtraction) recorded from a Cu (100) single crystal surface at two different take-off angles  $\theta$ . The surface and bulk peaks as resolved from simultaneous fitting of a series of photoelectron spectra are shown.

TABLE II. Surface to bulk intensity ratios  $k$  resolved from simultaneous fitting of a series of photoelectron spectra recorded from Cu single crystal surfaces at different photoelectron take-off angles  $\theta$  (see Section III.B for details).

$\theta$ ( $^{\circ}$ )	$k_{(111), \text{annealed}}$	$k_{(100), \text{annealed}}$	$k_{(110), \text{annealed}}$	$k_{(111), \text{damaged}}$
20	0.95	0.87	0.41	0.63
30	0.50	0.63	0.59	0.51
45	0.74	0.60	0.30	0.45
60	0.47	0.50	0.43	0.57

The results for the sputter-clean surface demonstrate the importance of a perfect surface structure. Thus, only in experiments with a well-defined single crystal surface layer, is it possible to determine a reliable value of the SCLS. In this context it is noted that surfaces of polycrystalline materials are also not suitable for determination of a value of the SCLS due to (i) the contribution of subsurface layers for various orientations, (ii) the possible differences in photoemission peak parameters between different orientations, and (iii) the presence of grain boundaries, in particular for the case of thin films where the grain size is usually very small.

## **B. Asymmetry and broadening of surface peaks: (111) and (100) Cu surfaces**

The measured asymmetry parameters for Cu (111) and (100) surfaces show the same behavior as was found in the 5d transition series<sup>1,3</sup> and for alkali metals,<sup>4</sup> i.e. higher surface singularity index as compared to the bulk singularity index. It can be shown, that the singularity index depends on the screening charge as follows:<sup>19</sup>

$$\alpha = \sum_l \frac{q_l^2}{2(2l+1)}, \quad (4)$$

where  $q_l$  is the partial screening charge, i.e. the amount of charge screening the core-hole with orbital momentum  $l$  (for the screening of a single core-hole it holds:  $\sum_l q_l = 1$ ). The values of the singularity index are within the range from 0 to 0.5. The maximum value is reached for a solely s-like ( $l = 0$ ) screening charge. With increasing contribution of p- or d-wave scattering the singularity index decreases. Thus, the rise in the singularity index at the surface reflects the decrease in momentum of the screening charge. For example, reduced sp-hybridization at an alkali metal surface is thought to be responsible for a sharp rise of the surface singularity index.<sup>4</sup> The values of the singularity index for Cu (111) and (100) surfaces obtained in this work (Table III) approach 1/18 – the minimum value for screening electrons with s, p and d symmetry. The bulk value of the singularity index is closer to zero indicating a decreased role of s or p-like electrons in screening a core-level hole within the bulk.

TABLE III. Surface core-level shift (SCLS), broadening  $\gamma$  and singularity index  $\alpha$  of surface and bulk peaks resolved from simultaneous fitting of a series of photoelectron spectra recorded from Cu single crystal surfaces (see Section III.B for details).

Cu surface	SCLS (eV)	$\gamma_{bulk}$ (eV)	$\alpha_{bulk}$ (a.u.)	$\gamma_{surface}$ (eV)	$\alpha_{surface}$ (a.u.)
(100), recovered	-0.35(5)	0.52(2)	0.00(2)	0.44(3)	0.06(3)
(111), recovered	-0.35(5)	0.51(2)	0.00(1)	0.45(3)	0.04(3)
(110), recovered	-0.36(6)	0.52(2)	0.01(2)	0.45(4)	0.03(4)
(111), sputter-cleaned	-0.33(7)	0.53(3)	<sup>a)</sup>	0.43(5)	0.09(7)

<sup>a)</sup> - reached the physically allowed lower limit of zero.

A reduction of the core-level line broadening of  $0.07 \pm 0.03$  eV is observed when the photoelectrons are emitted from the surface of both Cu (111) and (100), see Table III. Such a line broadening reduction has not been reported for 4d and 5d transition metals, instead broader surface peaks were observed.<sup>1-3</sup> The interpretation of the Cu  $2p_{3/2}$  photoemission peak broadening is not straightforward because several components including lifetime and phonon broadening, and subsurface contribution may have played a role.

### C. Surface core-level shifts for (111) and (100) Cu surfaces

The surface core-level shifts of metallic surfaces can be related to thermo-chemical parameters such as surface segregation energies and the work of adhesion. The equivalent core approximation (based on the assumption that the screening of a core-level hole effectively increases the positive charge of a nucleus by one) is used to relate the photoelectron surface core-level shift ( $SCLS_Z$ ) of a metal with atomic number  $Z$  to the surface segregation energy of an impurity with atomic number  $Z+1$  in that metal (with atomic number  $Z$ ).<sup>20</sup>

$$SCLS_Z = E_{surf} - E_{bulk} = \gamma_{Z+1 in Z}^{surf.segr}, \quad (5)$$

where  $E_{surf}$  and  $E_{bulk}$  are the core-level electron binding energies of the surface and bulk atoms respectively,  $\gamma_{Z+1 in Z}^{surf.segr}$  is the segregation energy of impurity  $Z+1$  from the bulk  $Z$  to the

surface. Segregation energies can be estimated using either *ab initio* calculations (linear muffin-tin orbitals method<sup>21,22</sup>) or with a semi-empirical macroscopic atom model.<sup>8,23</sup> The advantage of using a macroscopic atom model, as compared with *ab initio* calculations, is that it can be easily applied to complex systems. Development of this method is therefore important for applied materials science.<sup>24,25</sup>

For Cu, the  $SCLS_Z$  is related to the segregation of Zn (the Z+1 impurity) from the bulk to the Cu surface. The *ab initio* calculations for surface segregation energy of Zn in Cu results in  $-0.24$  eV for Cu (111) and  $-0.19$  eV for Cu (100) surfaces, but with an uncertainty up to  $0.2$  eV.<sup>22</sup>

In the macroscopic atom model the segregation energies depend on the surface energies and interfacial enthalpies as follows:<sup>8</sup>

$$\gamma_{A \text{ in } B}^{surf, segr} = \gamma_A^{surf} - \gamma_B^{surf} - (1 - f_{B \text{ surf}}^A) H_{A \text{ in } B}^{int} \quad (6)$$

Here  $H_{A \text{ in } B}^{int}$  is the enthalpy of mixing of metal  $A$  in metal  $B$ ,  $f_{B \text{ surf}}^A$  indicates the degree of contact of the Wigner-Seitz (WS) cell of the  $A$  impurity with surrounding  $B$  neighbors at the surface of  $B$ , the same factor within the bulk of  $B$  is equal to 1. The values of  $H_{A \text{ in } B}^{int}$  are also determined with the macroscopic atom model and are given in Ref. 8. The surface segregation energy of Zn in Cu becomes:

$$\gamma_{Zn \text{ in } Cu}^{surf, segr} = \gamma_{Zn}^{surf} - \gamma_{Cu}^{surf} - (1 - f_{Cu \text{ surf}}^{Zn}) H_{Zn \text{ in } Cu}^{int} \quad (7)$$

The surface energy (per surface atom) of a pure metal can be estimated<sup>8</sup> with:

$$\gamma_A^{surf} = f_{vacuum}^{<A>} c_0 (\gamma^* V^{\frac{2}{3}}) - RT, \quad (8)$$

where  $\gamma^*$  is the atomic interface energy between metal  $A$  and a vacuum,  $V$  the molar volume at temperature  $T$ ,  $c_0$  the proportionality constant between the surface area of a mole of atomic cells and  $V^{\frac{2}{3}}$  ( $c_0 = 4.5 \cdot 10^8$  in this work; the average of the values for a perfect sphere  $5.1 \cdot 10^8$  and a cube  $4.1 \cdot 10^8$ ) and  $f_{vacuum}^{<A>}$  is the fraction of the WS-cell's surface area exposed to vacuum. This last parameter depends on the type of the surface plane. For a fcc lattice the exposed fraction of WS-cell is fully determined by the missing nearest neighbors: e.g. for a (111) surface 3 out of the 12 neighbors are missing, thus  $f_{vacuum}^{<A>, (111)} = 1/4$ .

The segregation energy is mainly determined by the difference in the surface energies of two metals. The interface term usually accounts for no more than 20% of the total value of

the segregation energy. The surface energy in Eq. (8) depends on the values of  $\gamma^* V^{2/3}$ . These are obtained by extrapolating the surface energies of liquid metals to absolute zero or by using enthalpies of evaporation,<sup>8</sup> because no other means of obtaining surface energies for crystalline metals are available.

The experimentally determined surface core-level shifts for Cu (111) and (100) surfaces are shown in Table IV together with predictions based on *ab initio* calculations from Ref. 22 and the macroscopic atom model as discussed above. No dependence on the surface orientation of the surface core-level shift of Cu has been observed experimentally. The predicted values (from *ab initio* calculations and the macroscopic atom model) however suggest surface orientation dependence, but the uncertainty in these values is too large to be conclusive. The uncertainty for the surface core-level shift as obtained by *ab initio* calculations has a maximum value of 0.2 eV.<sup>22</sup> The uncertainty of these values estimated with macroscopic atom model is about 0.3 eV. The agreements and discrepancies between values for the surface core-level shift obtained experimentally and predicted with *ab initio* calculations and macroscopic atom model will be discussed next.

TABLE IV. Surface core-level shifts (SCLS) of Cu (111) and (100) single crystal surfaces according to model calculations and determined experimentally.

Method	SCLS <sub>(111)</sub> (eV)	SCLS <sub>(100)</sub> (eV)
ab initio calculations (Ref. 22)	-0.24±0.2	-0.19±0.2
macroscopic atom model	-0.18±0.3	-0.24±0.3
experiment	-0.35±0.05	-0.35±0.05

The SCLS values for close-packed single crystal surfaces of 5d transition metals i.e. (111) for fcc and (110) for bcc, as measured and predicted by both *ab initio* calculations and the macroscopic atom model are compared in Fig. 3. These metals show rather narrow photoelectron peaks and the surface contribution can be resolved easily as a completely separate surface peak is present in most cases, provided that sufficient energy resolution is utilized (usually achieved by applying synchrotron radiation). Agreement within 0.1-0.2 eV exists between the SCLS values according to *ab initio* calculations (Ref. 5 and references therein) and those determined experimentally. Differences of 0.2-0.3 eV occur when

comparing the SCLS values estimated on the basis of macroscopic atom model (Eqs. [6] and [8]) with the experimentally determined values for the 5d transition metals.

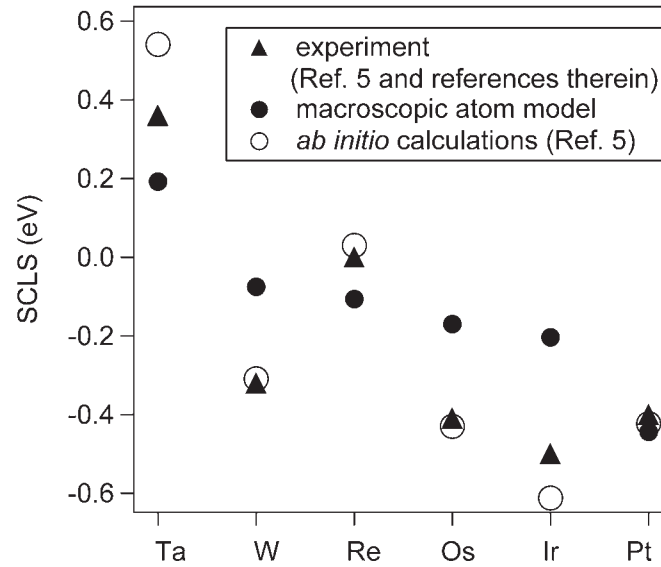


Fig. 3. Measured and calculated values for the surface core-level shifts (SCLS) of the close-packed single crystal surface of 5d transition metals, i.e. (111) for fcc and (110) for bcc.

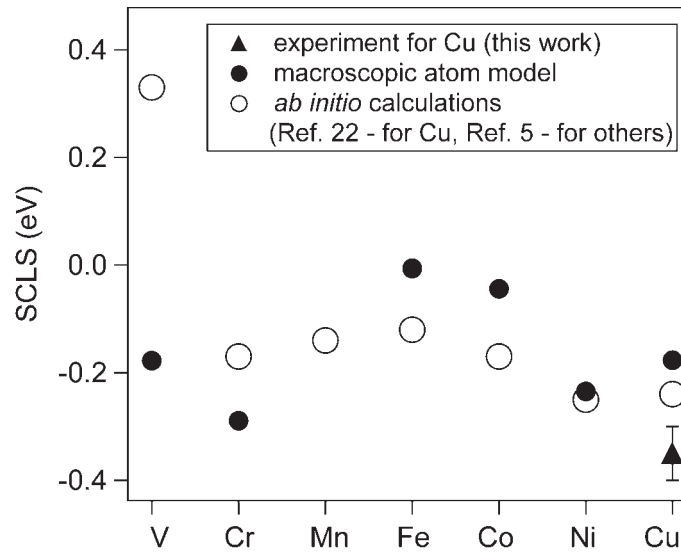


Fig. 4. Measured and calculated values for the surface core-level shifts (SCLS) of the close-packed single crystal surface of 3d transition metals, i.e. (111) for fcc and (110) for bcc.

A similar comparison of the SCLS values is made for the close-packed single crystal surfaces for 3d transition metal series, i.e. (111) for bcc and (110) for bcc, see Fig. 4.



However, in this case an experimental result is only available for Cu, which is obtained in this work. The values for the SCLS as estimated by both *ab initio* calculations and the macroscopic atom model are about 0.1 eV higher when compared with the experimentally determined values (cf. Table IV). This is well within the estimated uncertainty range of 0.2-0.3 eV. The large discrepancy for V can be explained by the relatively sharp drop in molar volume for the next (Z+1) element, i.e. Cr. Data for Mn are not considered because of its complicated crystallographic structure. To confirm the trend seen for SCLS values from the both *ab initio* calculations and the macroscopic atom model (Fig. 4), experimental data of other metals of the 3d series are required.

## V. CONCLUSIONS

A method for experimental determination of surface core-level photoemission shifts in 3d metals was demonstrated using copper as an example. The method is based on the analysis of the angular dependence of photoemission spectra. It was shown that a well-defined single crystal surface is a necessary condition for a successful determination of surface core-level shift. The experimentally determined values of the SCLS for Cu ( $-0.35 \pm 0.05$  eV) are within the uncertainty range (0.2-0.3 eV) of both *ab initio* calculations and the macroscopic atom model predictions for surface segregation energies of Zn in Cu. The method of SCLS determination for a 3d transition metal demonstrated here together with evolving theoretical descriptions can help understanding of the thermo-chemical properties of metallic surfaces and interfaces and allow development of the methods for prediction of the adhesion properties.

## ACKNOWLEDGEMENTS

This work was carried out under project number MC7.00075C in the framework of the Strategic Research Program of the Netherlands Institute for Metals Research in the Netherlands.

## REFERENCES

- 1 D.M. Riffe, G.K. Wertheim and P.H. Citrin, Phys. Rev. Lett. **63**, 1976 (1989).
- 2 D.M. Riffe and G.K. Wertheim, Phys. Rev. B **47**, 6672 (1993).
- 3 D.M. Riffe, W. Hale, B. Kim and J.L. Erskine, Phys. Rev. B **51**, 11012 (1995).
- 4 G.K. Wertheim, D.M. Riffe and P.H. Citrin, Phys. Rev. B **45**, 8703 (1992).
- 5 M. Aldén, I.A. Abrikosov, B. Johansson, N.M Rosengaard and H.L Skriver, Phys. Rev. B **50**, 5131 (1994).
- 6 B. Johansson and N. Martensson, Phys. Rev. B **21**, 4427 (1980).
- 7 N. Mårtensson, A. Stenborg, O. Björneholm, A. Nilsson and J.N. Andersen, Phys. Rev. Lett. **60**, 1731 (1988).
- 8 F.R. de Boer, R. Boom, W.C.M. Mattens, A.R. Miedema and A.K. Niessen, *Cohesion in Metals* (Elsevier Science Publishers, Amsterdam, 1988), Vol. 1.
- 9 P.H. Citrin, G.K. Wertheim and Y. Baer, Phys. Rev. B **27**, 3160 (1983).
- 10 M. Mehta and C.S. Fadley, Phys. Rev. Lett. **39**, 1569 (1977).
- 11 ASTM standard E902-88, Surf. Interface Anal. **17**, 889 (1991).
- 12 N. Fairley, in *Surface Analysis by Auger and X-ray Photoelectron Spectroscopy*, edited by D. Briggs and J.T. Grant (IM Publications, 2003), p. 397.
- 13 S. Doniach and M. Sunjic, J. Phys. C **3**, 385 (1970).
- 14 G.A. Somorjai, *Introduction to Surface Chemistry and Catalysis* (Wiley-Interscience Publication, New York, 1994).
- 15 S. Tanuma, C.J. Powell and D.R. Penn, Surface and Interface Analysis **17**, 911 (1991).
- 16 J. Osterwalder, in *Surface Analysis by Auger and X-ray Photoelectron Spectroscopy*, edited by D. Briggs and J.T. Grant (IM Publications, 2003), p. 557.
- 17 S. Tougaard, Surface and Interface Analysis **11**, 453 (1988).
- 18 S. Tougaard and P. Sigmund, Phys. Rev B **25**, 4452 (1982).
- 19 P.H. Citrin, G.K. Wertheim and Y. Baer, Phys. Rev. B **16**, 4256 (1977).

- 20 J.N. Andersen, O. Björneholm, A. Stenborg, A. Nillson and C. Wigren, J., Phys.: Condens. Matter **1**, 7309 (1989).
- 21 A. Christensen, A.V. Ruban, P. Stoltze, K.W. Jacobsen, H.L. Skriver, J.K. Nørskov and F. Besenbacher, Phys. Rev. B **56**, 5822 (1997).
- 22 H.L. Skriver (private communication); <http://databases.fysik.dtu.dk/hlsPT>.
- 23 R. Benedictus, A. Böttger, and E. J. Mittemeijer, Phys. Rev. B **54**, 9109 (1996).
- 24 L.P.H. Jeurgens, W.G. Sloof, F.D. Tichelaar, E.J. Mittemeijer, Phys. Rev. B **62**, 4707 (2000).
- 25 I.J. Bennett, J.M. Kranenburg and W.G. Sloof, J. Am. Ceram. Soc. (accepted for publication).
- 26 J.J. Kolodziej, T.E. Madey, J. W. Keister and J. E Rowe, Phys. Rev. B **62**, 5150 (2000).

## CHAPTER III

# GRAIN COALESCENCE AND ITS EFFECT ON STRESS AND ELASTICITY IN NANOCRYSTALLINE METAL FILMS

N.R. Shamsutdinov, A.J. Böttger, and B. J. Thijsse.

*Department of Materials Science and Engineering, Delft University of Technology,*

*Rotterdamseweg 137, 2628 AL Delft, The Netherlands*

## ABSTRACT

An approach based on the grain coalescence mechanism is developed to explain and predict the elastic behavior (and stress) of nanocrystalline films. The model explains how under an external strain coalescence and de-coalescence at grain boundaries alter the stress state of the film, thereby reducing the film's effective Young's modulus. An assessment of the effect of coalescence at grain boundaries could be made on the basis of the analysis of the contributions of grain boundary and strain energies. The estimations of Young's modulus and stress based on the model are in agreement with the data experimentally observed for sputtered iron nanocrystalline films.

## I. INTRODUCTION

The mechanical properties of nano-structured materials are of great importance for applications, as modern technology involves miniaturization. It is now well established that both plastic and elastic properties of nanocrystalline films significantly differ from their bulk counterparts (see Refs. 1,2 for reviews). During the past decades several investigations were dedicated to the observation and interpretation of elasticity and stress in thin nanocrystalline metal films. The observed elastic modulus in such films is often considerably lower, up to 30% less than the bulk value, and the intrinsic stress can exceed the bulk yield stress by an order of magnitude.

The anomalous elastic properties are considered to be the result of grain boundary phenomena, such as grain boundary sliding (GBS),<sup>3</sup> micro-cracking<sup>4</sup> or enhanced grain boundary compliance.<sup>5</sup> The GBS mechanism is based on the assumption of the inability of grain boundaries to sustain strong shear stresses. As a result, the stress under external uniaxial straining redistributes in such a way that the Young's modulus of a film is effectively reduced. However, there are experiments where a suppressed Young's modulus is observed under biaxial loading (see Ref. 6 and section III of this work). In these cases shear stresses are involved only through inhomogeneity, and therefore little effect of GBS is expected,<sup>5</sup> suggesting that other mechanisms alter the elastic behavior. The micro-cracking mechanism requires considerable grain boundary damage to be present in the material, for example, as much as one third of all grain boundaries should be fully detached in order to explain a 20% Young's modulus reduction in copper.<sup>4</sup> So this mechanism does not seem to provide a thorough explanation for the modulus reduction; it also cannot account for the observed time-dependence of the anomalous elasticity in thin films (see Ref. 7 for details). The third mechanism suggested in literature,<sup>5</sup> i.e. enhanced grain boundary compliance, considers grain boundaries as a second phase with different properties. As a result of this division in two separate phases, this model's predictions depend on the grain boundary thickness and on elastic properties of the grain boundary phase, which are both not measurable parameters and rather arbitrarily assigned. Up to now there is no common agreement on the dominant mechanism behind the elastic properties of nanocrystalline metallic films.

Considerable progress was achieved in explaining the development of the intrinsic tensile stress in nanocrystalline films through the so-called grain coalescence process.<sup>8-10</sup> Initially, the tensile intrinsic stress problem was addressed by employing the 'grain boundary

shrinkage' model. This model, developed in early 70s, attempts to view the intrinsic stress as determined solely by the morphology of the film.<sup>11</sup> Then the stress is determined as a result of the grain's elastic distortion (shrinkage) by  $\delta$ :

$$\sigma = \frac{E}{1-\nu} \frac{\delta}{2a}, \quad (1)$$

where  $2a$  is the typical grain size,  $E$  denotes the bulk Young's modulus and  $\nu$  is the Poisson ratio. The straightforward energy-based estimations of  $\delta$  failed to match the experimental values of intrinsic tensile stress. This led to the necessity to introduce the atomistic-based model grain boundary potential to explain the observed stress.<sup>11</sup> However, the parameters of this potential were not confirmed experimentally.

The grain coalescence-based approach to describe the development of tensile stress during the initial stages of film growth by Nix and Clemens<sup>8</sup> uses basically the same idea (as expressed in Eq. (1)) of tensile stress generation through the elimination of excess volume. In their approach the equilibrium between the stored elastic energy and the energy of grain boundary formation from free surfaces is analyzed. This leads to a simple relation between the geometry of grains and the generated intrinsic tensile stress. The model overestimates the stress, because plastic deformation is ignored and the choice of the geometry of the grains is rather particular (recent developments based on this model have led to more realistic stress values<sup>9</sup>). The proposed analysis, however, provides a viable physical background for estimations of intrinsic tensile stress in thin nanocrystalline films (see discussion in Ref. 10).

Inspired by these developments, the idea of coalescence-determined mechanics to describe *both* stress *and* the elastic properties of a nanocrystalline film on a substrate is employed in this chapter. In the original model<sup>8</sup> of Nix and Clemens the films consist of islands of elliptical shape, in the current analysis the films have a flat surface. Based on the results of the coalescence model the expected elastic behavior of such a system is analyzed. Both stresses and elastic modulus of a film can be estimated simultaneously as a function of film morphology (grain size, distribution of excess volume) and material constants such as bulk elastic properties, surface and grain boundary energies. It will be shown that the model proposed here successfully describes anomalous elasticity in polycrystalline thin films.

## II. COALESCENCE MODEL FOR FILMS WITH COLUMNAR GRAIN MORPHOLOGY

The grain coalescence model describes the interplay between the energy contributions of surfaces (free surface and grain boundary) and elastic energy as the excess free space in a thin film system changes. Since the excess free space distribution is of importance, the general film morphology considered in this work will be discussed first.

Morphologies for which it is likely that grain coalescence may affect mechanical properties are those that contain appreciable excess free space as is for instance the case for sputtered metal films of columnar morphology that generally contain (nano)-voids along the grain boundaries (see Fig. 1 and section 2 in Ref. 2).

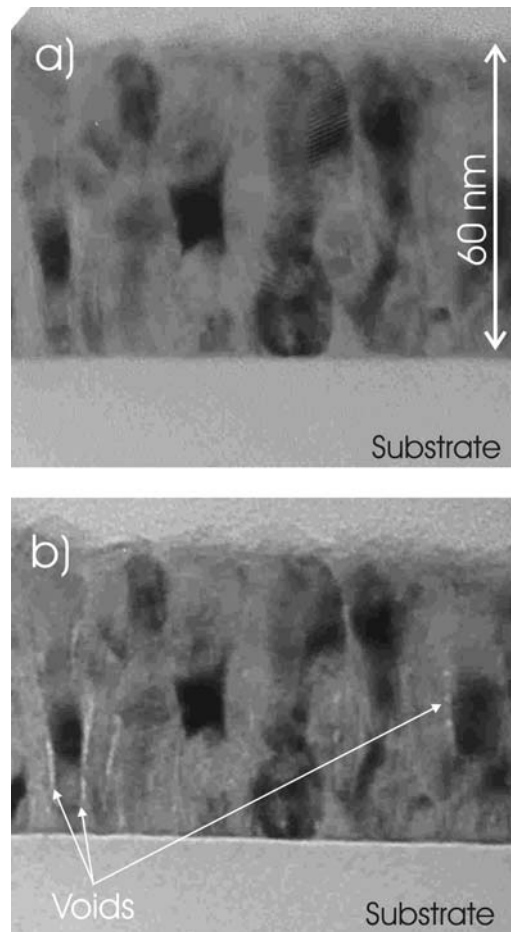


Fig. 1. Focused (a) and unfocused (b) transmission electron microscopy image of a cross-section of an as-prepared sputter deposited Fe-film on oxidized Si substrate. The imaging conditions allow outlining the interfaces through Fresnel-fringes; the substrate-film interface and nano-voids (see arrows) are visible. The overall grain morphology is columnar.

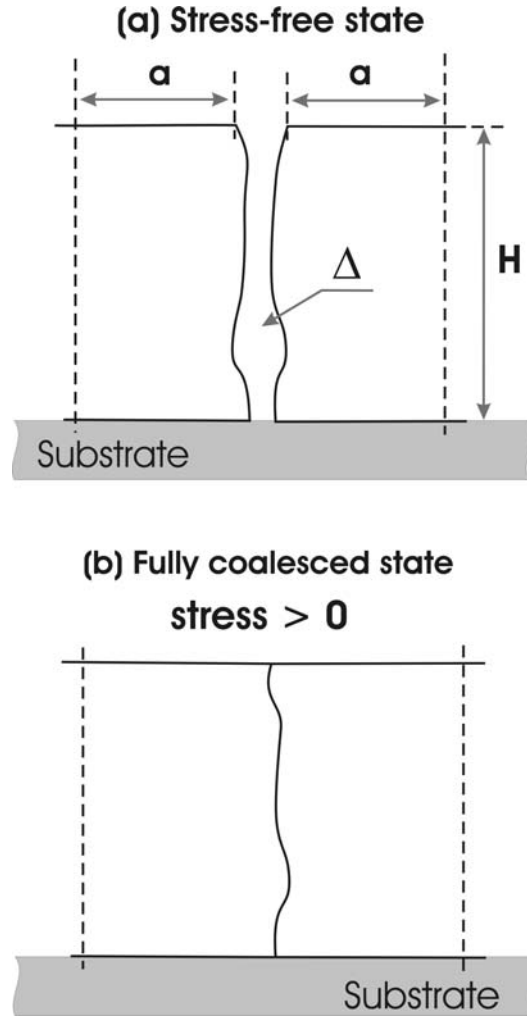


Fig. 2. Simplified model of a thin polycrystalline film on a substrate in two hypothetical states: (a) in the stress-free state, i.e. before coalescence, and (b) fully coalesced. In each picture two half-grains are shown, approximately acting as a ‘unit cell’ of the complete film. See text for  $a$ ,  $H$  and  $\Delta$ .

As a model system columnar-grained films with a flat surface will be considered. The latter implies that grain boundary grooving and surface roughness are regarded as small compared to the film thickness, i.e. these surface energy contributions are considered negligible.

As a simplified model system an array of grains of identical size  $2a$  and height  $H$  (Fig. 2) is taken. The grain size refers here to the average value; local variations of grain size will be neglected. For the sake of simplicity the material is taken to be isotropic, i.e. the elastic constants, surface and grain boundary energies are independent of crystallographic orientation. Initially, the system is considered without any interaction between grains, which implies that, if there are no other stress-generating mechanisms (such as an external load), the



grains are stress-free. In this hypothetical state grains are separated from each other by an inter-granular spacing  $\Delta$ , which can vary from grain to grain and along a given grain boundary. The inter-granular spacing is a measure of the excess volume along grain boundaries. The distribution of excess spacing,  $\eta(\Delta)$ , where  $\eta$  is the probability density of finding a spacing  $\Delta$  at any point along all grain boundaries, represents the film's morphology. The distribution of excess spacing is taken normalized:

$$\int_0^{+\infty} \eta(\Delta) d\Delta = 1. \quad (2)$$

In the hypothetical stress-free state, i.e. assuming total separation of grains as illustrated in Fig. 2(a), the free energy per unit film volume,  $F_1$ , is:

$$F_1 = (2\gamma_s)/a + 1/2 \cdot k \cdot \varepsilon^2 E / (1-\nu), \quad (3)$$

where  $\gamma_s$  is the surface free energy,  $2a$  is the in-plane grain size. Note that the energy contributions of the top surface and the bottom interface are neglected. The second term in Eq. (3) represents the elastic energy due to an externally applied strain  $\varepsilon$ . The factor  $k$  indicates what part of the strain is transferred from the substrate to the grain: if the grain's aspect ratio is low, i.e.  $H \ll a$ , then  $k$  can be taken equal to 1 (the strains in grain and substrate are equal), while narrow free-standing columns ( $a \ll H$ ) correspond to  $k = 0$  (negligible strain is transferred from the substrate to the column). The external strain  $\varepsilon$  is introduced here to investigate the linear response of the system, at the end of the analysis  $\varepsilon$  will be set to zero.

Next, we consider the same model system, but now in a hypothetical state in which the grains are fully coalesced, as shown in Fig. 2(b). Then the grain side surfaces are connected to each other, thereby forming closed grain boundaries, and the free energy per unit film volume,  $F_2$ , becomes:

$$F_2 = (\gamma_{gb})/a + 1/2 \cdot (\varepsilon + \Delta/2a)^2 \cdot E / (1-\nu), \quad (4)$$

The strain energy now consists of two contributions: (i) the external strain  $\varepsilon$  and (ii) the coalescence driven strain  $\Delta/2a$ .  $\gamma_{gb}$  denotes the grain boundary energy. Remark that the factor  $k$  is equal to 1 in this case, because in this fully coalesced state the external strain is fully transferred to the film material regardless of the aspect ratio.

To continue the analysis we consider a system for which partial coalescence occurs (Fig. 3). We assume that the coalescence occurs for the parts of the grain boundaries where  $\Delta$

is lower than some critical value  $\Delta_c$ , whereas for the inter-granular spacing larger than the critical value no coalescence occurs. If we ignore the stress fields between the coalesced and uncoalesced parts and in the mid-region of the grains (Fig. 3(b)), then the coalesced part of material is described by Eq. (3), and Eq. (4) represents the energy of the uncoalesced part. The consequences of this assumption will be discussed in section IV.

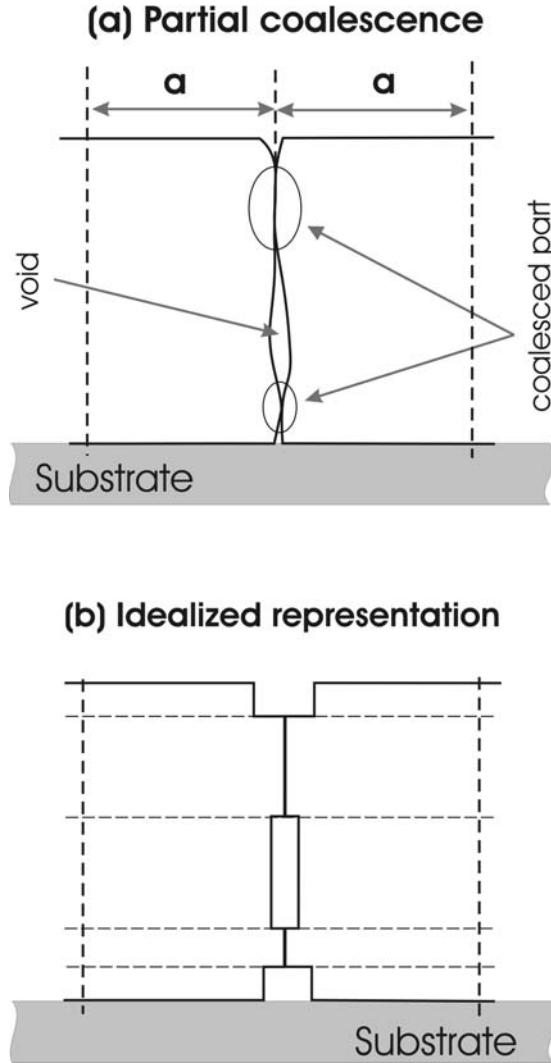


Fig. 3. (a) Two partially coalesced grains and (b) their idealized representation.

It is suitable to proceed further using a measure of coalescence  $g$  taken to be equal to the ratio of the surface area of coalesced grain boundaries to the total grain boundary surface area in the material. Obviously,  $g$  is zero when grains are totally separated and becomes 1 in case of full coalescence. Then the energy per unit film volume,  $F$ , is given by:

$$F = (1 - g)F_1 + g \langle F_2 \rangle_g \quad (5)$$

Here the second term, the coalesced part, is an average over the  $\Delta$  distribution in the coalesced part and depends on  $g$  as follows,

$$\langle F_2 \rangle_g = \int_0^{\Delta_c} \left[ \frac{\gamma_{gb}}{a} + \left( \varepsilon + \frac{\Delta}{2a} \right)^2 \left( \frac{1}{2} \right) \frac{E}{1-\nu} \right] \eta(\Delta) d\Delta \quad (6)$$

Here we have used the relation between the ratio  $g$  and the distribution of inter-granular spacing  $\eta(\Delta)$ :

$$g = \int_0^{\Delta_c} \eta(\Delta) d\Delta \quad (7)$$

$\Delta_c$  is the critical value of inter-granular spacing for which coalescence will occur, i.e. gaps with smaller spacing close, while those with larger spacing do not. To obtain the dependence of coalescence on an external strain  $\varepsilon$ , the energy of the film has to be extended as follows:

$$F = (1-g) \left( \frac{2\gamma_s}{a} + \frac{k\varepsilon^2 E}{1-\nu} \left( \frac{1}{2} \right) \right) + \int_0^{\Delta_c} \left[ \frac{\gamma_{gb}}{a} + \left( \varepsilon + \frac{\Delta}{2a} \right)^2 \left( \frac{1}{2} \right) \frac{E}{1-\nu} \right] \eta(\Delta) d\Delta \quad (8)$$

Further, we will assume that the coalescence is reversible, i.e. if the critical value  $\Delta_c$  changes, the material reacts by coalescence/decoalescence in a reversible manner. The value of  $\Delta_c$  is obtained by considering the equilibrium level of coalescence, i.e. the minimum of the energy of the film with respect to the ratio  $g$ . It is obtained by solving  $\left( \frac{\partial F}{\partial g} \right)_{\varepsilon, \eta(\Delta)} = 0$ :

$$\Delta_c(\varepsilon) = 2a \left( \sqrt{k\varepsilon^2 + 2 \frac{1-\nu}{E} \frac{(2\gamma_s - \gamma_{gb})}{a}} - \varepsilon \right) \quad (9)$$

Expression (9) is an extension of a similar formula obtained by Nix and Clemens.<sup>8</sup> Note the independence of the critical spacing  $\Delta_c$  on the distribution  $\eta(\Delta)$ . The dependence of  $g$  on  $\eta(\Delta)$  and  $\varepsilon$  is given by Eq. (7).

As an example the behavior of the critical spacing  $\Delta_c$  with varying  $\varepsilon$  for  $k=1$  is shown in Fig. 4 for the case of pure bcc Fe ( $E=211$  GPa,  $\nu=0.29$ ,<sup>12</sup>  $\gamma_s=3.3$  J/m<sup>2</sup>,<sup>13</sup>  $\gamma_{gb}=1/3\gamma_s$ ) and grain sizes ( $2a$ ) of 50 and 100 nm. The curves for  $k=0$  are not shown since they are almost indistinguishable from those for  $k=1$ . However, this does not imply that the factor  $k$  is not important. As will be demonstrated below, this factor plays an important role in the determination of the elastic properties. Fig. 4 shows, as expected, that coalescence is

suppressed under tensile loading i.e. the critical spacing  $\Delta_c$  is lower under applied tension than under compression. The critical spacing increases for larger grain size. This is due to the shift of the energy balance towards a coalesced state for larger grains (compare Eqs. (3) and (4)).

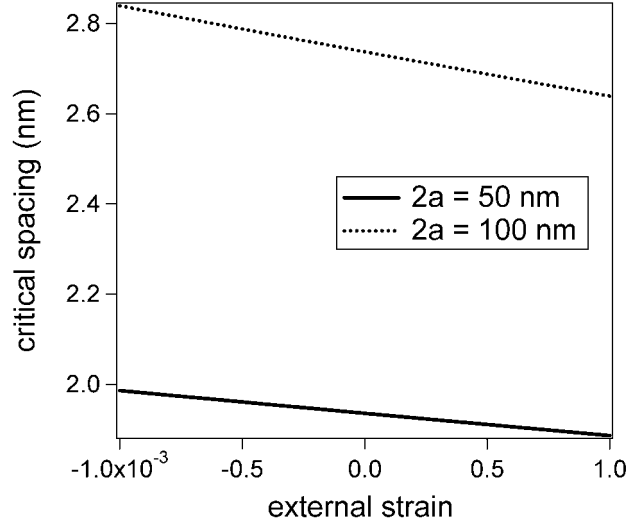


Fig. 4. Dependence of the critical spacing  $\Delta_c$  on an externally applied strain according to Eq. (9) for  $k=1$  and two grain sizes: 50 and 100 nm. The level of coalescence is reduced under tension and enhanced under compressive external strain. Larger grain size also promotes coalescence.

On the basis of the previous analysis a general relation between elastic properties and film stress, and the film's morphology (grain size and excess volume distribution) can be obtained. An estimate of the internal stress in the film is made by the derivation of Eq. (8) by strain  $\varepsilon$ . For zero external strain the expression for the (internal) film stress is reduced to

$$\sigma(\varepsilon = 0) = \left. \frac{dF}{d\varepsilon} \right|_{\varepsilon=0} = \left( \frac{E}{1-\nu} \right) \frac{1}{2a} \int_0^{\Delta_{c,0}} \Delta \eta(\Delta) d\Delta, \quad (10)$$

with  $\Delta_{c,0}$  the critical inter-granular spacing at zero strain:  $\Delta_{c,0} = 2a \sqrt{2 \frac{1-\nu}{E} \frac{(2\gamma_s - \gamma_{gb})}{a}}$ . The integral in Eq. (10) gives the average eliminated spacing (excess free space) divided by the grain size, which is equal to the average strain. Subsequently an expression for the Young's modulus of the film can be obtained through

$$E_{film}(\varepsilon = 0) = (1-\nu) \left. \frac{d^2 F}{d\varepsilon^2} \right|_{\varepsilon=0} \quad (11)$$

By means of differentiation of Eq. (8) and subsequently setting the external strain  $\varepsilon$  to zero, the Young's modulus is given by:

$$E_{film}(\varepsilon = 0) = E \left[ g + k(1 - g) - \eta(\Delta_{c,0}) \sqrt{8a \left( \frac{1 - \nu}{E} \right) (2\gamma_s - \gamma_{gb})} \right] \quad (12)$$

The equations for internal film stress and Young's modulus, Eqs. (10) and (12) respectively, obtained by considering energy equilibrium, relate the stress and elastic properties of a nanocrystalline film to its morphology. The last term in Eq. (12) corresponds to the grain coalescence mechanism. If it is ignored, then we arrive at the description of the passive role of inter-granular cracks.

From Eq. (12) it is obvious that the film's Young's modulus cannot exceed the bulk value, so a nanocrystalline film can become only more compliant than bulk material. In the case that  $\eta(\Delta_{c,0}) = 0$  and  $k=1$ , i.e. if no inter-granular gaps with spacing close to the critical value  $\Delta_c$  are present and all strain is transferred from the substrate to the film, the Young's modulus is equal to the bulk value. Note that also a film consisting of fully separated islands with  $k=1$  has the bulk Young's modulus according to the initial expression (3) for the energy of the hypothetical uncoalesced state. In the case that  $\eta(\Delta_{c,0}) > 0$ , the Young's modulus reduces due to grain coalescence/decoalescence and the reduction of  $E$  depends on the grain size and on the density of excess spacing around the critical value of  $\Delta_c$ . The distribution of excess space larger than the critical value does not influence the elasticity, only the gaps smaller than  $\Delta_c$  affect the stress (see Eq. (10)). In the following section the results of the grain coalescence model will be compared with experiments on Fe films.

### III. EXPERIMENTAL RESULTS

An experimental investigation of the state of stress and the elastic behavior is carried out on magnetron sputtered Fe thin films. The films have been deposited at room temperature on thermally oxidized 2-inch Si wafers. The deposition conditions are described elsewhere (Ref. 14 and Chapter IV of this thesis). The thickness of the films ranges from 50 nm to 400 nm and was determined by weighting before and after deposition and by assuming bulk bcc iron density. X-ray diffraction scans show that the films are single-phased:  $\alpha$ -Fe(bcc). The grain morphology of the as-sputtered films is columnar with the majority of the grains

spanning from the substrate to the top (Fig. 1). Under- and over-focused bright field transmission electron microscopy (TEM) images indicated the presence of very narrow voids along some grain boundaries (Fig. 1). The average in-plane grain size increases with the distance from the substrate. Scanning electron microscopy analysis of the surfaces allowed estimating the dependence of the in-plane grain size on the layer thickness (Fig. 5).

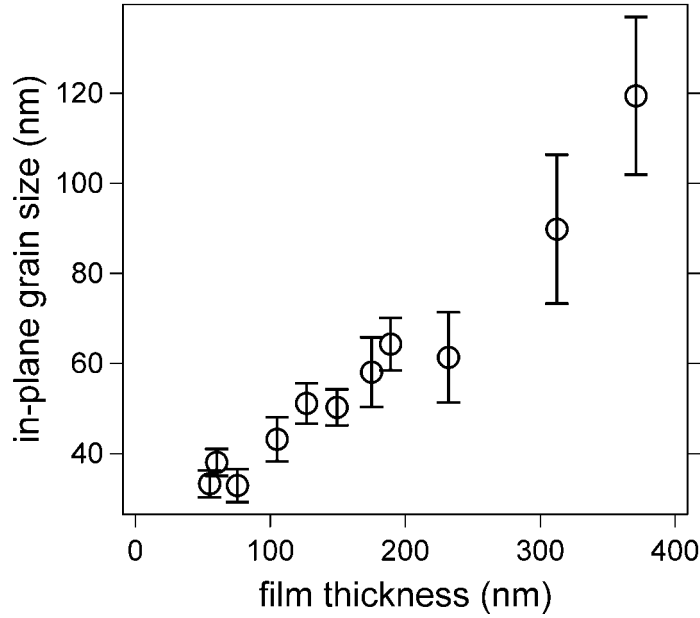


Fig. 5. In-plane grain size as a function of layer thickness for magnetron sputtered Fe films.

To monitor the stress evolution with temperature, the wafer curvature technique has been applied (FSM 900TCvac system). The thermal cycling experiments were performed in consecutive steps: up to 130 °C, 250 °C, 350 °C, 400 °C and 450 °C, with a heating/cooling rate below 2 °C/min. During such an experiment the effect of temperature can lead to thermally activated (diffusion) processes, as well as to a mechanical load on the film, since the coefficients of thermal expansion (CTE) of the iron film and the silicon substrate differ significantly. At sufficiently low temperatures (we applied an upper limit of 250 °C for Young's modulus determination), thermally activated processes are weak, and predominantly the mechanical load due to the CTE mismatch is present. If only CTE mismatch is causing strain, a linear stress-temperature curve is observed, as expected (see Fig. 6). The slope of this part of the thermo-loading curve is described by the expression

$$\partial \sigma_{film} / \partial T = (\alpha_{Si} - \alpha_{film}) \cdot E_{film} / (1 - \nu_{film}), \quad (13)$$

where  $\alpha$  denotes the CTE, and  $E_{film}$  and  $\nu_{film}$  are the Young's modulus and Poisson's ratio of the film respectively. Thus, the slope of the stress-temperature plot at sufficiently low temperatures depends only on the CTE mismatch and the elastic modulus. CTE values are assumed to be equal to the bulk ones (here the values from Ref. 15 were used). On the basis of this, the Young's modulus of the film can be determined in a thermo-cycling experiment using Eq. (13).

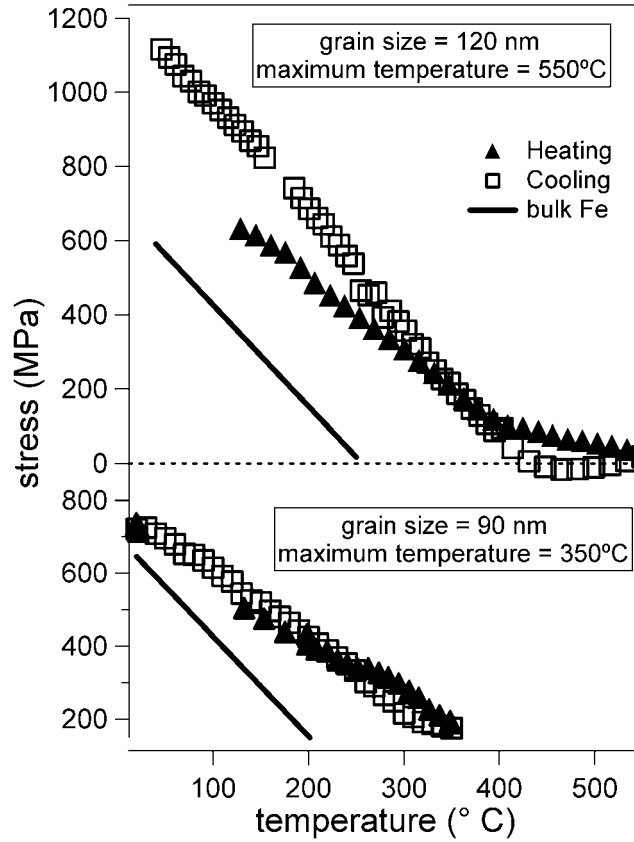


Fig. 6. Two typical stress-temperature curves. If high enough temperatures are reached, the film morphology changes, and the slope of stress-temperature curve during cooling becomes close to the slope calculated using the bulk bcc Fe elastic constants. If the film morphology is unchanged (at relatively low temperature), the slope of stress-temperature curve during cooling is virtually equal to that of the heating run, i.e. the elastic modulus remains smaller than the bulk value.

To justify the use of the method as described, an annealing experiment was performed in which a film was heated to a high enough temperature to cause grain growth (see Fig. 6). While the film remains nanocrystalline (during heating), its elastic modulus is decreased as compared to the bulk value. However, after the film morphology has changed at high temperatures (when grain growth is observed), the film shows bulk-like behaviour upon

cooling. If cooling starts at lower temperatures, then no difference in elasticity is observed between cooling and heating (Fig.6), indicating that no irreversible changes occur in the film. This experiment demonstrates that the determination of film thickness is sufficiently accurate, and justifies the use of the bulk values of parameters such as CTE.

X-ray diffraction pole figures reveal a weak fiber  $\langle 111 \rangle$ -texture in all films: the difference between the strongest and the weakest intensities is not more than a factor 2. The texture is practically constant over the thickness range of the films considered here. Transmission electron microscopy analysis indicates no microstructural differences (except grain size) between films of different thickness.

#### IV. DISCUSSION

The experimental results show that a very strong (up to 50%) reduction of the Young's modulus occurs (Fig. 7). Remarkably, the effect is more pronounced for the films with larger grains. This implies that mechanisms as GBS or grain boundary enhanced compliance cannot describe the observations. The GBS-mechanism is not occurring in this case, as it can explain neither the magnitude of the effect nor the dependence on grain size, because (i) the GBS predicts the reverse dependence on grain size<sup>7</sup> and (ii) the theoretical limit of the Young's modulus reduction through GBS-mechanism is calculated to be at most 38% for uniaxial loading,<sup>3</sup> and even smaller for biaxial loading. These predictions obviously do not match our experimental findings. Models that employ enhanced grain boundary compliance to explain the elastic behavior of thin films also fail to describe the observed grain size dependence. Since the volume fraction of the 'grain boundary phase' should rapidly decrease with increased grain size, enhanced compliance would decrease for films of larger grain size, which is not observed here.

The coalescence model, however, could explain the observed trends, as will be shown next. To apply the coalescence model described in section II, the morphology, i.e. the grain size and the shape of excess space distribution  $\eta(\Delta)$  in a film, should be addressed (see Eqs. (8), (10) and (12)). Whereas grain size is a measurable parameter, the distribution  $\eta(\Delta)$  is difficult to determine experimentally in a direct manner. The parameter related to excess volume is the film's density (or the density deviation from the bulk). The film-bulk density



difference can be expressed in terms of the ratio  $V_{\text{excess volume}}/V_{\text{total}}$ , which is related to  $\eta(\Delta)$ , but does not uniquely define the distribution  $\eta(\Delta)$ :

$$\frac{V_{\text{excess volume}}}{V_{\text{total}}} = \int_0^{\infty} \frac{\Delta}{2a} \eta(\Delta) d\Delta \quad (14)$$

An approximation of the shape of the distribution  $\eta(\Delta)$  can be obtained by analyzing the two main factors that can affect it: the first one is the trend towards the energy minimum, and the second one is formed by the limitations of purely geometrical origin such as non-matching grain or void shapes (caused by the deposition conditions) and the strength of the attachment of the grain to the (rigid) substrate.

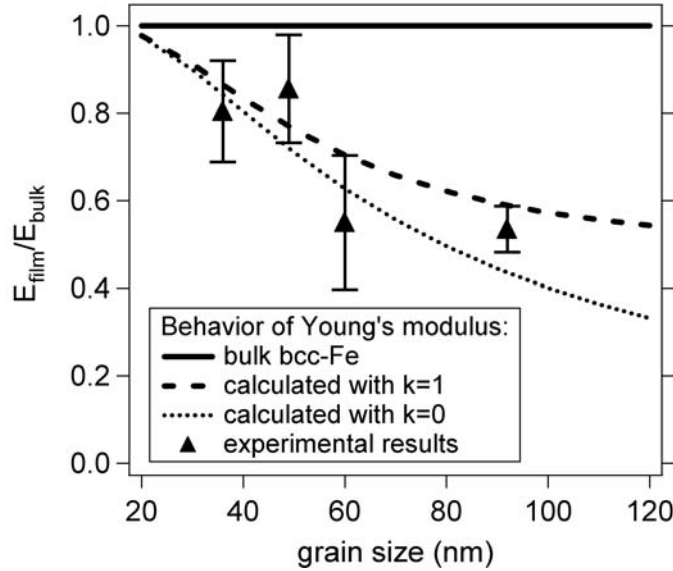


Fig. 7. Measured Young's modulus in Fe films and calculated values assuming the Gaussian excess space distribution of Eq. (15) with the width parameter set to 2% of the grain size.

First, let us consider the hypothetical state of the film for which there are no geometrical limitations: weak attachment to the substrate, and grains of shapes that perfectly match each other. The distribution  $\eta(\Delta)$  can change to minimize the energy of the system as expressed by Eq. (8), and the energy minimum is achieved when  $\eta(\Delta)$  is equal to a  $\delta$ -function around  $\Delta = 0$  plus some free volume of spacing larger than  $\Delta_c$ . The latter is required to preserve the density if the boundaries of the film are fixed (see Eq. (14)). For further consideration the free volume with gaps larger than  $\Delta_c$  can be ignored, since it does not affect stress or elasticity (see Eqs. (10) and (12)).

Second, let us consider the case that grains are fixed by a rigid substrate and that grains have shapes that do not necessarily match with the neighboring grains. These constraints prevent the development of the excess space distribution into a  $\delta$ -function. A distribution of the excess space as a broader peak function with the center around zero is a suitable representation of the system. The function describes both the distribution of excess volume to obtain a minimum of energy of the system and accounts for the geometrical limitations. In what follows a Gaussian will be considered as the distribution of excess space:

$$\eta(\Delta) = \frac{2}{w\sqrt{2\pi}} \exp\left(-\frac{\Delta^2}{2w^2}\right), \quad \Delta \geq 0 \quad (15)$$

Here  $w$  is the width parameter of the Gaussian.

This distribution will be used to estimate the magnitude of the effect of excess volume on the Young's modulus. To preserve the same density in films of different grain sizes (this is to compare to the experimental data, which did not reveal any microstructural changes with increased grain size), the width parameter  $w$  of the distribution of excess space must be proportional to the grain size. Let us set the width parameter  $w$  of the distribution to 2 % of the grain size. Using this, the Young's modulus (Eq. (12)) for bcc-Fe films ( $E=211$  GPa,  $\nu=0.29$ ,  $3\gamma_{gb}=\gamma_s=3.3$  J/m<sup>2</sup>) is given in Fig. 7 for two limiting cases: for  $k=1$  and  $k=0$ . The calculated reduction of Young's modulus is strong and reaches 40% for  $k=1$ . The trend shown in Fig. 7 also demonstrates that the Young's modulus decreases with an increase of grain size. This trend is a consequence of the increasing (with grain size) importance of the volume contribution (elastic energy) to the total energy as compared to the interface contribution (energy of surfaces/grain boundaries). As a result, the material with larger grains decoalesces easier.

Moreover, the coefficient  $k$  is expected to reduce with film thickness. For example, for the Fe films investigated here the width of a columnar grain increases while the area attached to the substrate remains the same. Thus, an even stronger drop in Young's modulus with increasing grain size can be expected. Exactly this trend is observed in the experimental values of  $E$  (Fig. 7). To our knowledge the observed trend cannot be explained employing other existing models.

It is interesting to discuss the asymptotic behavior of the Young's modulus calculated using the described coalescence model and the excess volume distribution (15) with the width parameter  $w$  equal to 2 % of the grain size  $2a$ . As demonstrated in Fig. 8, for very large grain

sizes the coefficient  $k$  plays an important role. This is because the last term in Eq. (12) becomes negligible, i.e. the coalescence/decoalescence process is not important anymore. Now the factor  $k$  defines whether the film reacts to external strain as (i) bulk material would (for  $k=1$ ) or (ii) there is no reaction from the material due to an almost full separation of grains and the inability to transfer an external strain from substrate to the material ( $k=0$ ).

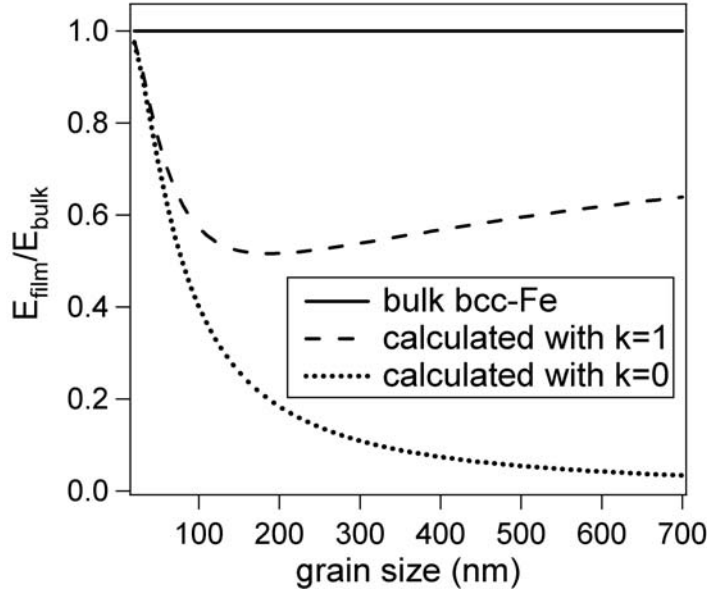


Fig. 8. The asymptotic behavior of the modeled Young's modulus in Fe films, assuming a Gaussian excess space distribution with the width parameter set to 2% of the grain size.

The fraction of excess volume ( $V_{\text{excess volume}}/V_{\text{total}}$ ) for the Gaussian excess space distribution (Eq. (15)) with a width parameter  $w$  of 2 % is equal to only 1.6%. TEM observations show that the Fe films indeed contain few narrow nano-voids (Fig. 1).

The tensile stress values in the film, estimated according to Eqs. (15) and (10) with the width parameter  $w$  equal to 2 % of the grain size  $2a$ , are shown in Fig. 9 together with the experimental values. The calculated values and the experimental data show the same trend. The calculations overestimate the magnitude of the effect, which is the result of assumptions such as neglecting the detailed strain field in individual grains and the application of a certain shape here (a Gaussian) for the excess volume distribution (by tuning this peak form, a better match with experiment can be obtained).

This analysis employs the simplest form of a coalescence model. If the strain field of the non-coalesced part is to be taken into account, the present analysis could in principle be repeated with adapted expressions for the elastic energies. Because any forms of the stress

state of a partially coalesced grain lead to a dependence of the critical spacing  $\Delta_c$  on the distribution  $\eta(\Delta)$ , this implies that the Young's modulus and stress dependence on grain size could be calculated only numerically. The resulting dependencies, however, will not differ qualitatively from the current analysis, because the Young's modulus and stress reduction with increasing grain size is related to the increased contribution of elastic energy. These general trends are well represented by the formulae (10) and (12). The presented results clearly demonstrate that the behavior of both stress and elasticity of thin films containing excess space can be understood using the coalescence model.

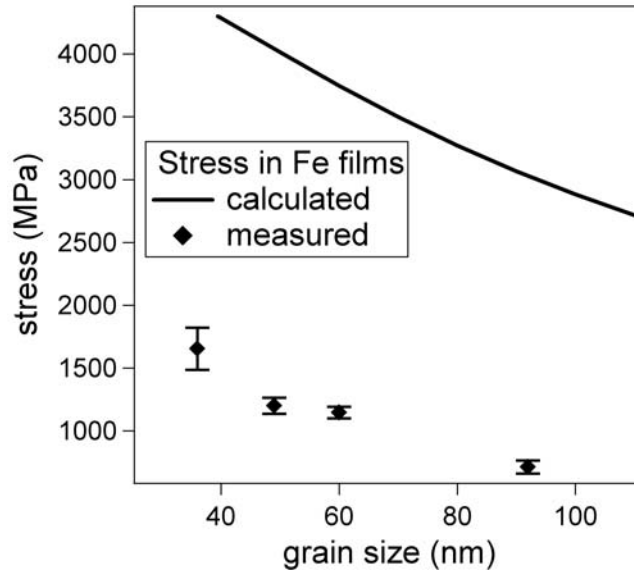


Fig. 9. The measured stress in Fe films and the estimates calculated according to Eq. (10) for a Gaussian excess space distribution (with the width set to 2% of grain size) show the similar trend in dependence on grain size. However, magnitude of the effect is overestimated.

The actual coalescence process involves some kinetic factors. In the present model, individual grains have to overcome certain energy barriers to (de-) coalesce and to come to an equilibrium state: before the energy gain is achieved, part of the grains need to stretch elastically. However, in a real nanocrystalline film the inter-granular voids have shapes of cracks (see Fig. 1). It is expected that at the tip of such a crack the energy barrier to overcome is relatively small, as such the tip can serve as a nucleation site of a “zipping” process at the inter-granular crack as described by Nix and Clemens,<sup>8</sup> thereby providing a fast mechanism for coalescence.

## 5. CONCLUSIONS

An approach based on an energetic analysis of the grain coalescence process can explain elastic properties and the occurrence of tensile stress in nanocrystalline thin films. The analysis shows that a reduction in elastic modulus as compared to the bulk value can be expected, and that the effect strongly depends on the morphology and grain size. The change of a film's Young's modulus with grain size predicted by the model agrees well with experimentally observed trends for Fe thin magnetron sputtered films of thickness below 400 nm.

## REFERENCES

- 1 S.C. Tjong, H. Chen, Materials Science and Engineering R **45**, 1 (2004).
- 2 K.S. Kumar, H. Van Swygenhoven, S. Suresh, Acta Mater **51**, 5743 (2003).
- 3 C. Zener, Phys. Rev. **60**, 906 (1941).
- 4 H. Huang, F. Spaepen, Acta Mater **48**, 3261 (2000).
- 5 P. Sharma, S. Ganti, J Mater Res **18**, 1823 (2003).
- 6 M.M. de Lima Jr., R.G. Lacerda, J. Vilcarromero, F.C. Marques, Journal of Applied Physics **86**, 4936 (1999).
- 7 A.J. Kalkman, A.H. Verbruggen, G.C.A.M. Janssen, Appl Phys Lett **78**, 2673 (2001).
- 8 W.D. Nix, B.M. Clemens, J Mater Res **14**, 3467 (1999).
- 9 S.C. Seel, C.V. Thompson, S.J. Hearne, J.A. Floro, J Appl Phys **88**, 7079 (2000).
- 10 L.B. Freund, S. Suresh, *Thin Film Materials. Stress, Defect Formation and Surface Evolution* (Cambridge University Press, Cambridge 2003), p.70.
- 11 F.A. Doljack, R.W. Hoffman, Thin Solid Films **12**, 71 (1972).
- 12 G.W.C. Kaye, T.H. Laby, *Tables of physical and Chemical Constants, 16th edition* (Longman, Harlow Essex 1995), p.44.
- 13 A.V. Ruban, H.L. Skriver, J.K. Nørskov, Phys. Rev. B **59**, 15990 (1999).
- 14 N.R. Chamsoutdinov, A.J. Böttger, R. Delhez, F.D. Tichelaar, Mat Res Soc Symp Proc **795** U11.23.1 (2004).
- 15 G.W.C. Kaye, T.H. Laby, *Tables of physical and Chemical Constants, 16th edition* (Longman, Harlow Essex 1995), p.73.

## CHAPTER IV

# **MECHANICAL PROPERTIES OF AND THE ROLE OF DISLOCATIONS AND GRAIN BOUNDARIES IN NANOCRYSTALLINE THIN LAYERS: THE CASE OF FE FILMS**

N.R. Shamsutdinov, A.J. Böttger, R. Delhez, N.M. van der Pers and F. D. Tichelaar

*Department of Materials Science and Engineering, Delft University of Technology,*

*Rotterdamseweg 137, 2628 AL Delft, The Netherlands*

### ABSTRACT

The relation between morphology and mechanical properties of nanocrystalline films, in this case magnetron sputtered iron films (grain sizes up to 100 nm), is studied. The macro- and micro-stress behavior dependence on grain size, porosity and heat treatment up to 400 °C is investigated and a method is developed to determine orientation distribution of dislocations from X-ray diffraction line profile analysis. The tensile stress and Young's modulus are observed to *increase* upon annealing in some of the films. The porosity, and reduced ability to relieve stresses by dislocation movement in nanocrystalline layers invokes a grain coalescence mechanism that leads to a stress and elastic modulus increase upon annealing. Combination of this mechanism with the more commonly observed stress relaxation by dislocation movement could explain the observed mechanical response.

## I. INTRODUCTION

Nanocrystalline metals offer abundant possibilities of application, and understanding the nature of their mechanical behavior is vital. The dependence of the yield strength on grain size of nanocrystalline materials deviates from the classical Hall-Petch relation for conventional polycrystalline metals.<sup>1,2</sup> Further, the reported results are often contradictory and up to now there is still ambiguity about the morphological features that influence the yield strength behavior.

To study the influence of grain size in many experimental studies on nanocrystalline materials annealing is applied. However, little is known about the effects that could occur (relaxation, diffusion) and their influence on the mechanical properties.

The aim of the present chapter is to investigate the relation between film morphology (changes) and mechanical properties. Iron sputtered thin films with grain sizes up to 100 nm are used as a model system to study the effects of annealing. In pure iron the diffusion-driven processes are slow at room temperature but already at relatively mild temperatures (400 °C) they become important. This circumstance allows the analysis of both the diffusion phenomena and purely mechanical mechanisms by considering the response of material to temperature changes.

In this work we combine various experimental techniques to monitor the properties of magnetron sputtered Fe films. X-ray diffraction  $\sin^2\psi$ -method and wafer curvature analysis are applied to track stress changes with annealing. Scanning and transmission electron microscopy are used for microstructure observations; these measurements provide accurate grain size characteristics and illustrate important morphological features such as the presence of voids.

An X-ray diffraction line width analysis is developed and applied to study the dislocation distributions in films. We demonstrate that the combined effect of large stress and annealing leads to annihilation of most of the dislocations with Burgers vector close to the direction of maximum resolved shear stress.

The gathered experimental evidence suggests that grain boundaries play an important role regarding the mechanical behavior of nanocrystalline thin metallic films.



## II. METHODS

### A. Film deposition, morphology, crystal structure and texture

Fe films are deposited on thermally oxidized 2-inch Si-wafers at room temperature using magnetron sputtering in a Leybold Z550 coater. The base pressure in this system is below  $7 \cdot 10^{-5}$  Pa and a working Ar-pressure of 4.8 Pa is used. The film growth rate applied is 3.1 nm/min. The layer thickness of the films, determined by weighing before and after deposition, ranges from 50 nm to 400 nm, assuming bulk bcc iron density.<sup>3</sup>

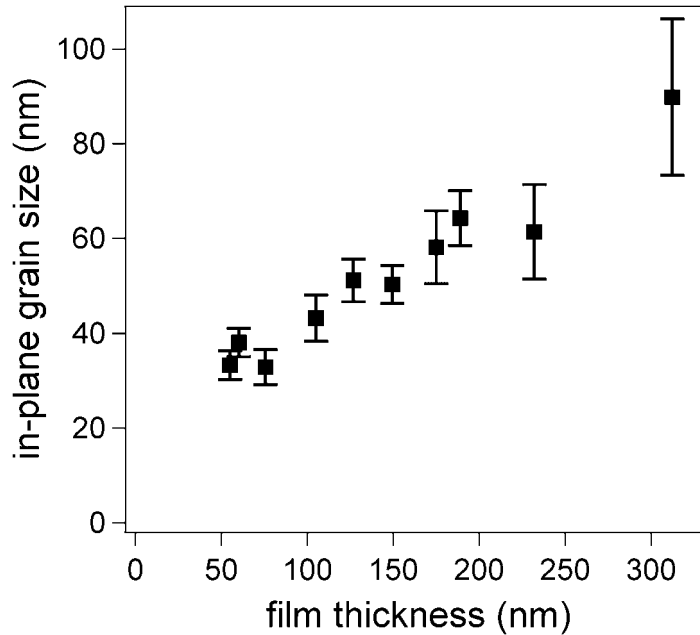


Fig. 1. In-plane grain size at surface of the as-deposited Fe films as a function of film thickness.

Scanning electron microscopy (using a JEOL JSM-6500F) analysis of surfaces is used as an estimate of the in-plane grain size dependence on the iron layer thickness (Fig. 1). The average in-plane grain size at the surface increases with film thickness. All the films used in this study are nanocrystalline, i.e. their in-plane grain size is below 100 nm (i.e. 35 nm - 100 nm). The microstructures of films are examined by a PHILIPS CM30T transmission electron microscope (TEM) operating at 300 kV. The grain structure appears to be columnar with grains spanning from the substrate to the top (see Fig. 2). Under- and over-focused bright field transmission electron microscopy images indicate the presence of very narrow, i.e. of the order of a nanometer, crack-like voids along some grain boundaries (Fig. 2).

X-ray diffraction (XRD) experiments are carried out using a Bruker-Nonius D5005 diffractometer mounted with a Co X-ray tube and a monochromator in the diffracted beam, yielding diffraction patterns that contain only Co  $K_{\alpha}$ -radiation. The diffraction patterns demonstrate that as-deposited films are single-phased:  $\alpha$ -Fe(bcc). XRD pole figures reveal a weak fiber  $\langle 111 \rangle$ -texture in all films: the difference between strongest and the weakest intensity is not more than a factor 2. For this reason the texture effects on stress and dislocation distribution analysis will be ignored below.

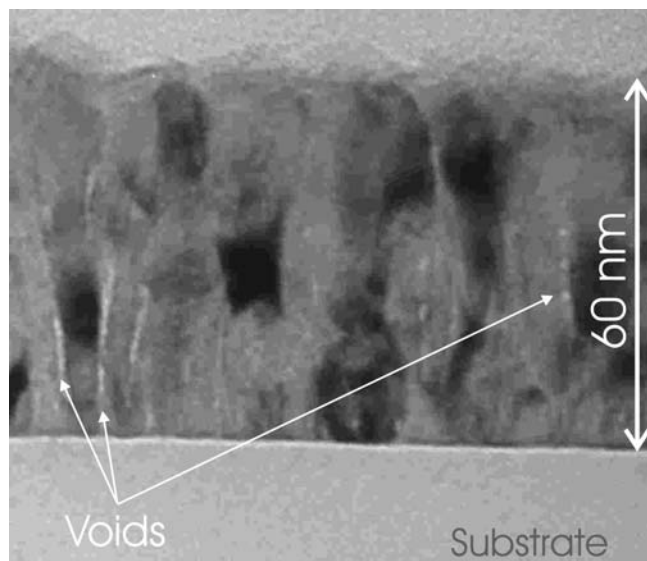


Fig. 2. Defocused bright-field TEM-image of an as-prepared 60 nm Fe-film. The interfaces, i.e between the Fe-film and substrate or Fe and nano-void, are outlined by Fresnel- fringes.

## B. Stress evolution with temperature and Young's modulus determination

The stress as a function of temperature and as a result of an annealing treatment can provide valuable insight into the mechanical behavior of the material. During such an experiment the effect of temperature can lead to thermally activated (e.g. diffusion) processes, as well as to a mechanical load on the film, because the coefficients of thermal expansion of the film material and the substrate differ. The thermo-mechanical load experiment can be used to derive the film's Young's modulus which is an important parameter of the mechanical state of the films. The Young's modulus of thin films often differs from the bulk value due to the influence of voids or relatively large volume of grain boundary regions:<sup>2,4,5</sup>  $E_{film} \neq E_{bulk}$ .

The stress evolution is investigated by thermal cycling experiments performed inside a wafer curvature set-up (FSM 900TCvac system) in vacuum (below  $10^{-4}$  Pa) in consecutive steps: up to 130 °C, 250 °C, 350 °C, 400 °C and 450 °C, at each temperature annealing is sustained for 5 min. The heating/cooling rate is about 2 °C/min.

At sufficiently low temperatures (i.e. below 200 °C) thermally activated processes are essentially nonexistent and only mechanical load due to thermal expansion coefficients mismatch is present. This is demonstrated by the near-linearity and reversibility of a stress-temperature curve (see, for instance, Fig. 3). This allows determining Young's modulus as follows. The slope of the linear part of the thermal loading curve (i.e.  $\partial\sigma_{film}/\partial T$ ) is described by the expression

$$\partial\sigma_{film}/\partial T = (\alpha_{Si} - \alpha_{film}) E_{film}/(1 - \nu_{film}), \quad (1)$$

where  $\alpha$  denotes the coefficient of thermal expansion of the substrate or film,  $E_{film}$  and  $\nu_{film}$  are Young's modulus and Poisson's ratio of the film respectively.

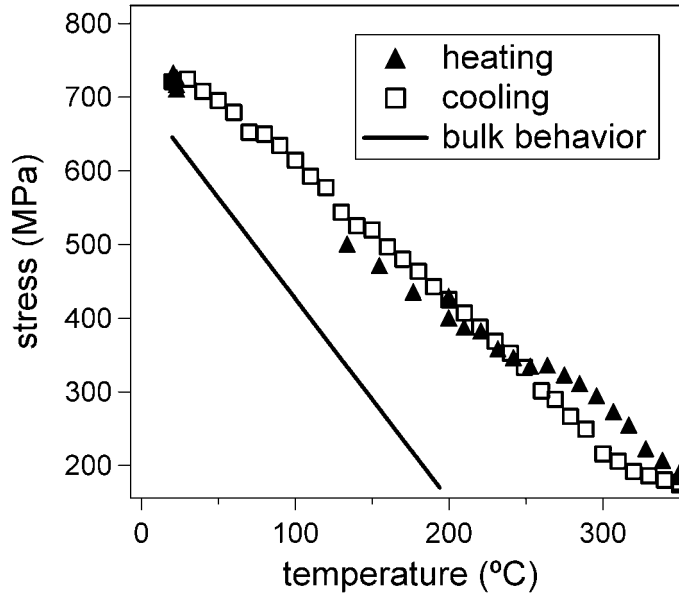


Fig. 3. Film stress evolution as a function of temperature obtained by wafer curvature measurements for the Fe film of 312 nm thickness. A linear behavior is observed up to 250 °C. The full line indicates the stress-temperature curve as expected for material with bulk elastic modulus. The cooling and heating rates applied are about 2 °C/min.

The thermal expansion coefficients are considered the same for bulk material and thin films,  $\alpha_{film} = \alpha_{bulk}$ , since the effects of microstructure on the thermal expansion coefficient

can be considered to be of minor importance for the stress development. By using the known (bulk) coefficients for thermal expansion ( $\alpha_{Fe}=11.8 \cdot 10^{-6} \text{ K}^{-1}$ ,  $\alpha_{Si}=2.6 \cdot 10^{-6} \text{ K}^{-1}$ ),<sup>6</sup> the Young modulus of the film can be determined in a thermal cycling experiment through Eq. (1). The Poisson's ratio of Fe is close to  $\frac{1}{3}$  and will be considered independent on morphology.

In this study Young's modulus is determined using cooling data starting from at most 200 °C to room temperature. The slope of the cooling curve below 200 °C is only weakly dependent on temperature (see example in Fig. 3). The difference with the slope expected for bulk material (solid line in Fig. 3) is much greater than this dependence.

### C. Micro-strain analysis

X-ray diffraction is applied to monitor the changes of the macro- and micro-strain after annealing runs. Here the macro-strains refer to the strains averaged over the diffracting volume, while the micro-strains describe the local strain variations: from grain to grain and within grains. The dislocation behavior can be investigated by analyzing the micro-strains.

Macro-strains are determined using the conventional  $\sin^2\psi$  stress analysis of X-ray diffraction patterns of the {211} and {220} Fe diffraction lines applying  $\omega$ -geometry.<sup>7</sup> Tilt angles  $\psi$  range from 2° to 45°. The stresses are calculated from the measured strains using the X'Pert Stress program of PANalytical with the X-ray elastic constants calculated according to Kröner-Eshelby.<sup>7</sup>

The micro-strains in the films are investigated on the basis of the integral breadths of diffraction lines using the measurements for the macro-strain determination. Correction for the instrumental broadening is performed through the measurement of a reference Al-specimen (99.99% purity, grain size < 5µm, made by Aluminium Powder Company) and the instrumental contribution is removed under assumption of Gaussian line shapes (application of a Cauchy shape did not qualitatively affect the results). The two remaining contributions to the line width are the effects of the limited size of crystallites and of the micro-strain. Both effects can be distinguished, since the grain geometry in this study is known from electron microscopy analysis. The size effect on the diffraction line broadening can be estimated according to the Scherrer formula (the approach described in Reference 8 is used in this work) and its contribution is subsequently removed from the observed peak widths using Gaussians to describe diffraction line profile shapes. This is justified because the

reconstructed size broadening accounted for no more than 10% of the total line width. The line breadth  $\beta_\varepsilon$ , remaining after removal of the instrumental and size broadening is attributed to micro-strain. The averaged micro-strain  $\langle \varepsilon \rangle$  in the film is obtained through:  $\langle \varepsilon \rangle = 1/4 \beta_\varepsilon \cot \theta$ ,<sup>8</sup> where  $\theta$  is the Bragg angle.

The averaged micro-strain is obtained from the same XRD data as those used in  $\sin^2 \psi$  stress analysis. Fig. 4 shows the typical behavior of the micro-strain as a function of tilt angle  $\psi$  for the  $\{211\}$  and  $\{220\}$  Fe reflections. It will be shown in Section III that in the Fe films investigated here dislocations are the predominant cause for the micro-strain. Now we will discuss how the anisotropy of micro-strain can be analyzed to obtain insight into the geometry of dislocations.

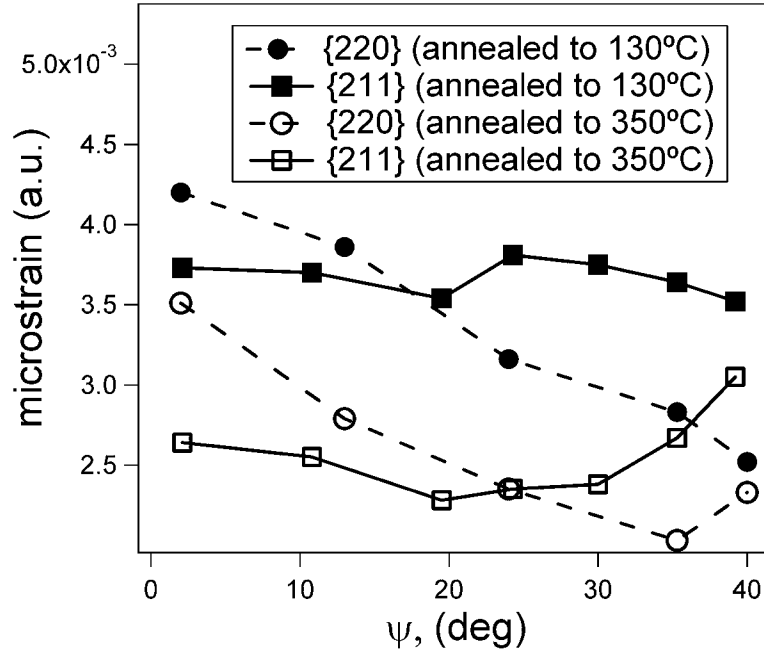


Fig. 4. Micro-strain as a function of specimen tilt angle  $\psi$  for the Fe film of 312 nm thickness when annealed to 130 and 350 °C. The clearly observed  $\psi$ - and hkl-dependence rules out elastically isotropic defects as the main cause of micro-strain.

The strain field  $\varepsilon$  of a dislocation can be converted into an integral breadth  $\beta_q^{calc}$  of a diffraction line profile with a scattering vector  $\mathbf{q}$  (using here micro-strain averaging as described in Reference 9) according to

$$\beta_q^{calc} = \left[ 2\sqrt{2\pi} \sqrt{\int |\varepsilon_q|^2 dV / V} \right] \tan \theta, \quad (2)$$

where  $\varepsilon_q$  is the strain in the direction of the scattering vector  $\mathbf{q}$ .

In Eq. (2)  $\beta_q^{calc}$  relates to the Gaussian that describes the diffraction line profile caused by micro-strains. Further, interactions between dislocations are not taken into account. These simplifications will not affect the discussed trends but could affect the absolute values of dislocation densities, which are probably underestimated here.

Because it is assumed that the dislocations do not interact, the whole material can be considered as consisting of non-interacting volumes containing only one dislocation. Then the dislocation density defines the size of this volume. The integration of the known  $\varepsilon_q$  field in Eq. (2) is performed over this volume. The dislocation density will be one of the parameters to be obtained by fitting of the line widths as will be described below. Here we applied the classical expression for a dislocation strain field,<sup>10</sup> which implies that the dislocation core region should be excluded from the integration in Eq. (2). In the present calculations the dislocation core-radius is set to  $3|\mathbf{b}|$ , where  $\mathbf{b}$  is the Burgers vector.

For the sake of simplicity only screw dislocations are considered, as mostly screw dislocations are observed in bcc metals.<sup>11</sup> In a given bcc crystallite there are 4 non-parallel Burgers vector orientations (of the  $\langle 111 \rangle$ -family). Then using Eq. (2), the broadening, caused by any arrangement of dislocations for a given diffraction vector  $\mathbf{q}$ , can be calculated.

The orientation distribution of dislocation is assumed to be rotationally symmetric on average, due to the rotationally symmetric deposition conditions, and the resulting rotationally symmetric film morphology. The orientation distribution of dislocations will be described by  $\rho_\chi$  - the density of screw dislocations with Burgers vector at angle  $\chi \pm \Delta\chi$  from the film's surface normal.  $\chi$  ranges from 0 to 90°, and a step ( $2 \cdot \Delta\chi$ ) of 10° is applied in the calculation. The diffraction broadening response ( $\beta_{q,\chi}^{calc}$ ) of the dislocations with Burgers vector at angle  $\chi \pm \Delta\chi$  from the surface normal for any scattering vector  $\mathbf{q}$  can be simulated by averaging over all possible crystallite orientations that diffract with this scattering vector and contain such dislocations. The measured dependence of X-ray diffraction line broadening ( $\beta_q^{exp}$ ) on tilt angle  $\psi$  (between  $\mathbf{q}$  and the surface normal) can now be fitted with  $\sqrt{\sum \rho_\chi^2 (\beta_{q,\chi}^{calc})^2}$ , and the distribution of screw dislocations densities ( $\rho_\chi$ ) can be found.

The effect of texture is not taken into account because the texture in the films is weak (see Section II.A). As an illustration of the absence of texture effects on micro-strain one can consider the evolution of micro-strain upon annealing (Section III): the micro-strains change considerably after annealing but no texture changes are observed.

### III. RESULTS

Here the results of the macro- and micro-stress evolution with annealing will be given. In this work we are interested in the effect of annealing on the system without changing its morphology. Above 400 °C the morphology changes considerably: the surface becomes flatter by diffusion and at temperatures higher than 500 °C also grain growth occurs. The grain size remains unchanged until at least 350 °C as indicated by electron microscopy observations. XRD measurements show that the texture does not change until this temperature either. Therefore only the results of annealing experiments up to 350 °C are reported here.

From the wafer curvature measurements the Young modulus is determined as described in Section II.B. The Young modulus of as-deposited films is initially significantly lower than the bulk value (Fig. 5). This phenomenon was reported previously for other nanocrystalline metallic films.<sup>2,4,5</sup> Upon annealing, however, the Young modulus evolves toward the bulk value. As for the stress evolution, a different behavior for the thinner and thicker films is observed, i.e. for the thicker films Young's modulus after annealing is still significantly lower than the bulk value.

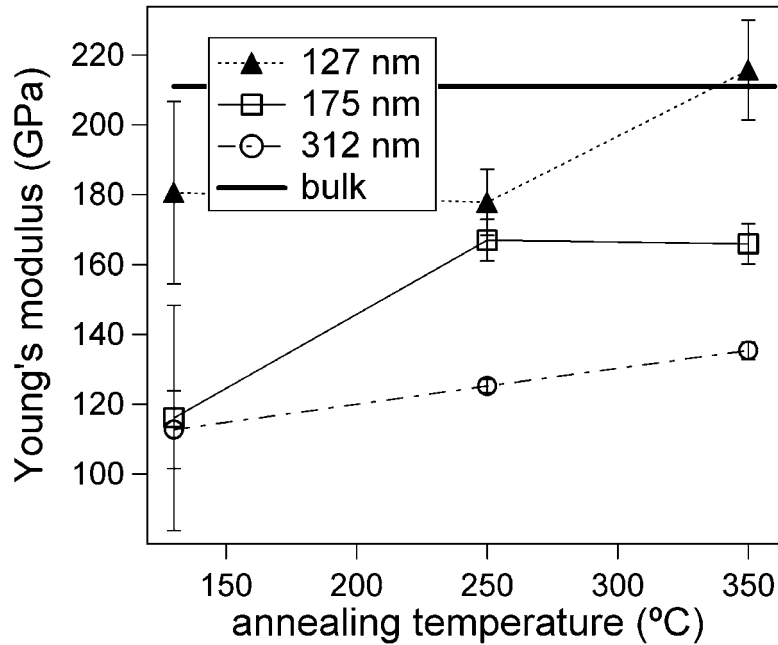


Fig. 5. Elastic modulus after annealing cycles up to 350 °C. All specimens show initially a Young modulus smaller than that of bulk material, an increase is observed upon annealing. The observed behavior is explained by the presence of nano-voids along grain boundaries (see Section IV).

The wafer curvature and X-ray stress analysis show that the stress states in the films are biaxial and rotationally symmetric. All stress values mentioned in this chapter will refer to stresses in the plane of the layer.

The evolution of the tensile macro-stress upon annealing as measured by XRD at room temperature is shown in Fig. 6. Although no large stress changes are observed until 350 °C, two trends could be observed: the stress in thinner films (i.e. 60 nm, 125 nm) slightly decreases and the stress in thicker films (i.e. 175 nm and 310 nm) slightly increases. The stress increase observed in thicker films is surprising as a stress decrease is expected due to plastic relaxation at higher temperature.

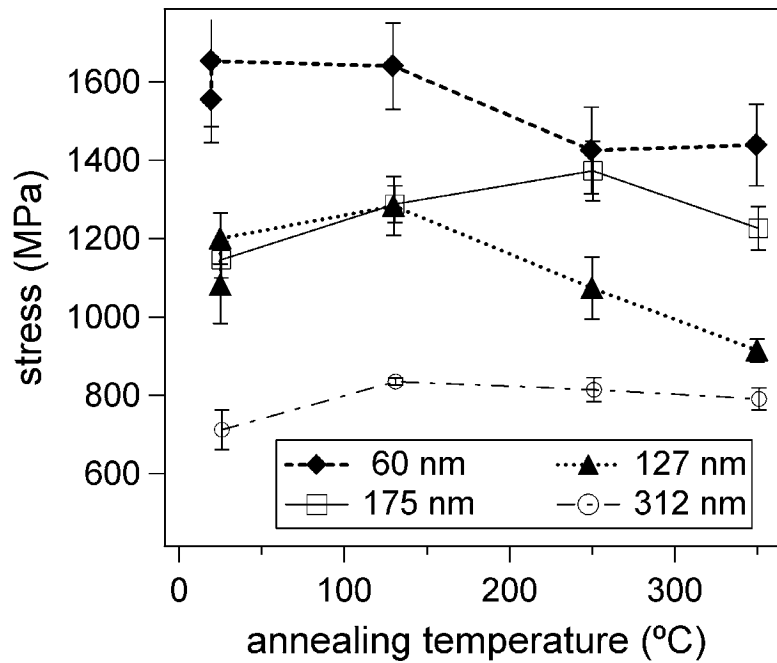


Fig. 6. Tensile stresses measured by XRD at room temperature after annealing cycles up to 350 °C. The thinner films (60, 127 nm) show a decrease of tensile stress upon annealing, whereas the thicker films show a slight increase of stress.

In order to obtain insight into the nature of the micro-strain and its evolution with annealing, the micro-strain dependence on the tilt angle  $\psi$  (see example in Fig. 4) is analyzed. First, we note that no decrease of micro-strain is observed towards the ‘stress-free’  $\psi$ -angle for biaxial stress-state ( $\psi_0=41^\circ$  for bcc iron).<sup>7</sup> This suggests that lattice defects are responsible for the micro-strain rather than a macro-stress gradient perpendicular to the surface. Further, the micro-strain shows a dependence on tilt angle. This rules out elastically isotropic defects, e.g. point defects, as a possible cause and suggests that dislocations are the



origin of the observed micro-strain behavior (stacking faults do not occur in bcc metals).<sup>11</sup> To investigate the evolution of the dislocation distribution the analysis of the diffraction line breadths as described in Section III.C is applied.

The overall dislocation density (as determined at room temperature by XRD-analysis) decreases with increasing annealing temperature (Fig. 7). Until 250 °C the decrease is gradual, a steeper drop occurs for annealing at temperatures somewhere between 250 °C and 300 °C.

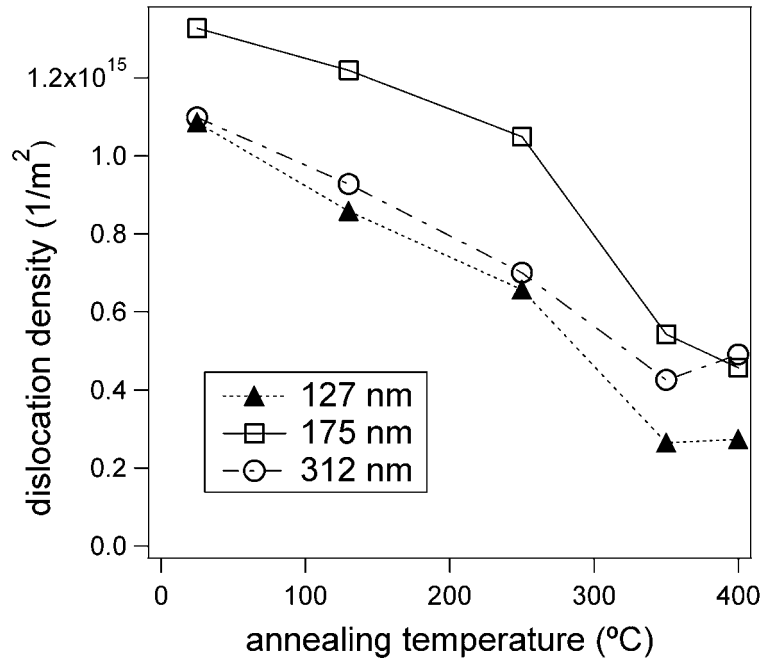


Fig. 7. Screw dislocation density determined for three thicknesses of the Fe films on the basis of room temperature XRD measurements after annealing cycles. Diffraction line widths of {211} and {220} reflections are used to estimate the dislocation density.

The analysis of the orientation distribution of dislocations suggests a remarkable evolution with annealing. Fig. 8 shows the screw dislocation density dependence on the angle between the Burgers vector and the surface of the film. The orientation distribution of dislocations is investigated for two films (with thickness of 175 nm and 310 nm). The orientation distribution of dislocations for the 175 nm film does not change shape with annealing, i.e. the dislocation density reduction proceeds in an isotropic way. The main feature of the shape of the distribution is a strong dislocation density reduction around 45 ° - the direction of maximum shear. On the other hand, for the 310 nm film a change of shape occurs after annealing to 250 °C: below that temperature no dislocation density reduction at

45 ° is observed. Thus, for this film, at 250 °C practically all screw dislocations with Burgers vector around the direction of maximum resolved shear stress disappear. Significant changes at temperatures higher than 250 °C can also be seen in thermal loading curves: usually deviations from linearity appear above this temperature (see example in Fig. 3).

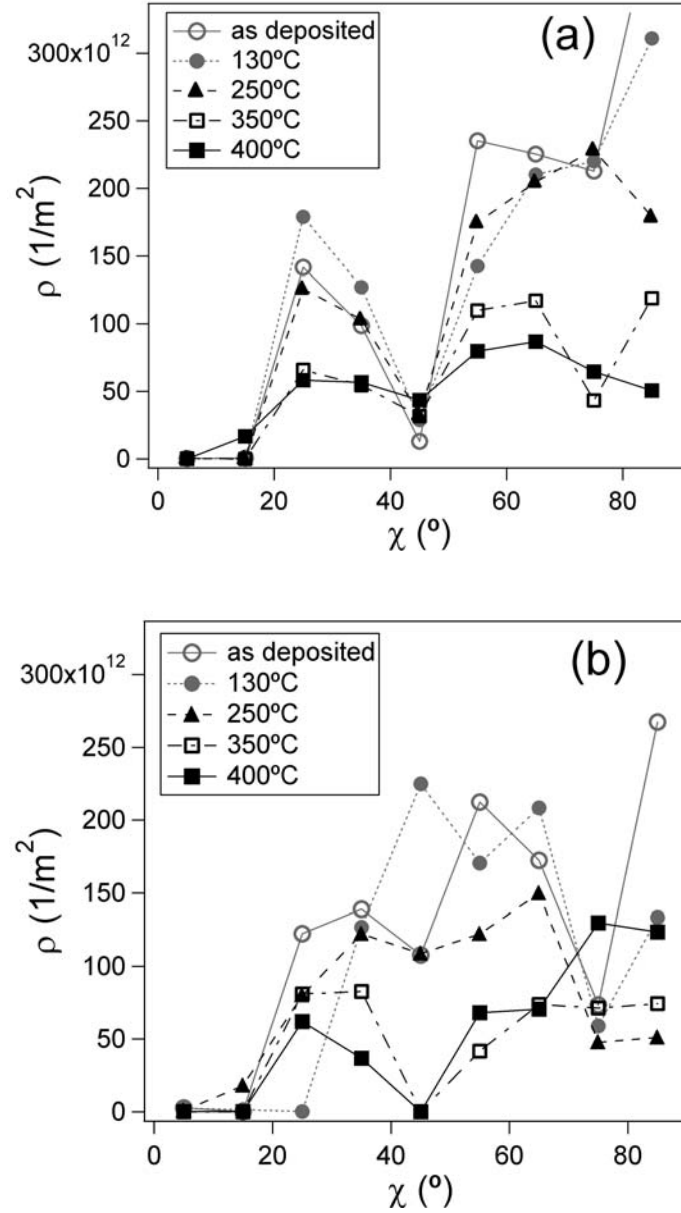


Fig. 8. Orientation distribution of the screw dislocation density in (a) 175 nm thick and (b) 312 nm thick Fe films at room temperature after annealing at 130 °C, 250 °C, 350 °C, and 400 °C (see Section II-B). The dislocation density is shown here as a function of the angle  $\chi$  between the Burgers vector and the film's surface normal.

## IV. DISCUSSION

Stress, elastic modulus, morphology and dislocation density of nanocrystalline Fe films were monitored as a function of annealing. To identify the processes behind the mechanical behavior of Fe films with annealing, the phenomena that are essentially bulk-like (dislocation-mediated plasticity) will be discussed separately from those related to grain boundaries (coalescence, grain boundary sliding).

The initial (pre-annealed) shape of dislocation orientation distribution (Fig. 8) suggests that the high stresses in the thinner film (approximately 1.1 GPa) cause the disappearance of the dislocations with Burgers vector along the direction of the maximum resolved shear stress. In the thicker film, which has been shown to be under a lower tensile stress of 0.7 GPa, however, these dislocations are abundant. After annealing above 250 °C almost all of these dislocations disappear from the thicker film (Fig. 8(b)), suggesting that the dislocation mobility greatly increases above this temperature. This is also supported by the observation of the onset of non-elastic behavior at that temperature in the stress-temperature curves (see wafer curvature experiment example in Fig. 3). Similar observations of annealing-caused annihilation of the dislocations with glide direction along the maximum resolved shear stress were obtained in a study of Ni thin films.<sup>12,13</sup>

If stresses at higher temperatures become compressive, then an overall stress increase is possible.<sup>14</sup> In our experiments, however, stresses as monitored by wafer curvature remain tensile within the temperature range used, i.e. plastic relief can result only in stress decrease. Indeed, for thinner films, weak stress relief is found as a result of annealing at temperatures higher than 150 °C. However, for annealing at temperatures lower than 150 °C and for annealing at higher temperatures for thicker films no stress changes are present as a result of annealing, even a weak stress increase occurs (Fig. 6). These observations suggest the presence of a mechanism that causes stress to increase.

The most obvious mechanism that can cause a film under tension to increase tensile stress is excess volume elimination. It can be shown, that it is energetically favorable to close narrow voids between grains, i.e. to reduce surface energy, to form a grain boundary at the cost of increasing the elastic energy.<sup>15</sup> In the films studied here the presence of narrow voids was detected by TEM analysis (Fig. 2).

Since even very little reduction of porosity can cause dramatic stress changes (just 0.1 % change of total porosity in iron increases the stress by about 0.1 GPa, as shown in Chapter III of this thesis and Ref. 16), obtaining a direct evidence of voids' closure is hard. But the presence of voids along grain boundaries affects other mechanical properties such as elasticity. The analysis of the evolution of Young's modulus upon annealing can help to illustrate that voids at grain boundaries do close.

The mechanisms, that are considered in literature to be responsible for the elastic modulus reduction in nanocrystalline films, are based on imperfect grain boundaries. Within the grain boundary sliding model<sup>17</sup> a grain boundary cannot sustain a shear stress; this can occur if such a grain boundary contains voids. Within the micro-cracking<sup>4</sup> or coalescence mechanism (Ref. 16 and Chapter III of this thesis) no full cohesion between grains is present, i.e. grain boundaries contain excess volume.

Regardless of the model employed to explain the observed behavior of Young's modulus (Fig. 5), a trend towards the bulk value with annealing is consistent with the suggestion that imperfect grain boundaries are gradually 'repaired'. This indicates that some excess volume along grain boundaries is eliminated during annealing, causing the tensile stress to increase. Annealing can cause inter-granular voids' closure either by (i) increased surface diffusion (for instance, filling the voids with material to a certain extent when coalescence becomes possible) or by (ii) reducing the tensile stress load on the material (due to thermal expansion coefficients mismatch between Si-substrate and the film) and thus promoting coalescence.

The processes of dislocation mediated stress relaxation and void elimination (although of quite different nature) are tightly related. Stress relaxation through plasticity reduces the elastic energy inside grains, i.e. grain coalescence is promoted (see Chapter III and Ref. 16). Estimations also show that the stress caused by coalescence can be extremely large.<sup>15,16</sup> If stress caused by coalescence exceeds the yield strength then the dislocation-mediated stress relief turns on.

The observed differences in stress evolution upon annealing for films of different thickness are most probably a result of the interplay between the two mechanisms. In thinner films the higher initial stresses suppress the coalescence processes and dislocation mediated plasticity relieves stresses. In thicker films the processes at grain boundaries (coalescence) become more prominent due to low initial stress level.

The observations made here are consistent with the increase of hardness in nanocrystalline iron as a result of annealing, observed in another investigation.<sup>18</sup> Initially, the material with imperfect grain boundaries is easier to deform, i.e. it shows lower yield strength. Upon annealing the grain boundaries are repaired (closed or coalesced) leading to an increase in tensile stress, yield strength and elastic modulus.

## **V. CONCLUSIONS**

The mechanical properties and the evolution of properties with annealing are studied for metallic nanocrystalline materials on the example of sputtered Fe thin films.

A method is developed and applied to analyze the orientation distribution of the dislocation density. It is shown that annealing of Fe thin films in a biaxial state of stress can lead to annihilation of dislocations with glide direction along the maximum resolved shear stress.

The evolution of tensile stress upon annealing cannot be explained solely by dislocation-mediated plasticity, and it is suggested that another process occurs that leads to an increase of tensile stress. On the basis of Young's modulus and morphology observations it is concluded that the mechanism of grain coalescence is responsible for this tensile stress increase.

The two mechanisms simultaneously affect the stress state of the thin nanocrystalline films. The first one – dislocation-mediated stress relief – acts within the interior of grains, while the second one – grain coalescence or elimination of excess space along grain boundaries – acts at grain boundaries. The interplay between the two mechanisms significantly affects the stress state of nanocrystalline metals and is crucial for understanding the mechanical properties of these materials.

## REFERENCES

- 1 K.S. Kumar, H. Van Swygenhoven, and S. Suresh, *Acta Materialia* **51**, 5743 (2003).
- 2 S.C. Tjong, and H. Chen, *Materials Science and Engineering R* **45**, 1 (2004).
- 3 G.W.C. Kaye, and T.H. Laby, *Tables of Physical and Chemical Constants*, 16 th ed., Longman, Harlow Essex, UK, 1995, p. 41.
- 4 H. Huang, and F. Spaepen, *Acta Materialia* **48**, 3261 (2000).
- 5 P. Sharma, and S. Ganti, *Journal of Materials Research* **18**, 1823 (2003).
- 6 G.W.C. Kaye, and T.H. Laby, *Tables of Physical and Chemical Constants*, 16 th ed., Longman, Harlow Essex, UK, 1995, p. 73.
- 7 V.M. Hauk, and E. Macherauch, *Adv. in X-ray Anal.* **27**, 81 (1983).
- 8 R. Delhez, T.H. de Keijser, J.I. Langford, D. Louër, E.J. Mittemeijer, and E.J. Sonneveld, *The Rietveld Method*, edited by R.A. Young, Oxford University Press, New York, NY, 1993, pp. 132-66.
- 9 Th.H. de Keijser, E.J. Mittemeijer, and H.C.F. Rozendaal, *J. Appl. Cryst.* **16**, 309 (1983).
- 10 D.Hull, and D.J. Bacon, *Introduction to Dislocations*, Butterworth-Heinemann, Oxford, UK, 2001, p. 65.
- 11 D.Hull, and D.J. Bacon, *Introduction to Dislocations*, Butterworth-Heinemann, Oxford, UK, 2001, p. 110.
- 12 J.-D. Kamminga, L.J. Seijbel, and R. Delhez: *Diffraction Analysis of the Microstructure of Materials*, edited by E.J. Mittemeijer and P. Scardi, Springer-Verlag, Berlin, Germany, 2004, pp. 309-31.
- 13 L.J. Seijbel, J.-D. Kamminga, and R. Delhez, *Materials Science Forum* **404-407**, 715 (2002).
- 14 R.-M. Keller, S.P. Baker, and E. Artz, *Journal of Materials Research* **13**, 1307 (1998).
- 15 W.D. Nix, and B.M. Clemens, *Journal of Materials Research* **14**, 3467 (1999).
- 16 N.R. Shamsutdinov and A.J.Böttger, submitted to *Acta Materialia*.
- 17 C. Zener, *Phys. Rev.* **60**, 906 (1941).

- 18 J.B. Savader, M.R. Scanlon, R.C. Cammaranta, D.T. Smith, and C. Hayzelden:  
Scripta Materialia **36**, 29 (1997).

## CHAPTER V

# **THE EFFECT OF CU INTERLAYERS ON GRAIN SIZE AND STRESS IN SPUTTERED FE-CU MULTILAYERED THIN FILMS**

N.R. Shamsutdinov, A.J. Böttger, F. D. Tichelaar

*Department of Materials Science and Engineering, Delft University of Technology,*

*Rotterdamseweg 137, 2628 AL Delft, The Netherlands*

### ABSTRACT

The stress states of magnetron sputtered Fe-Cu multilayered thin films are studied using X-ray diffraction, in particular with respect to the relation between stress and morphology. The deposition of copper interlayers between layers of iron can lead to the formation of epitaxial bcc Cu which can keep the orientation of iron crystallite unchanged through the whole thickness of a multilayer. Copper interlayers are also demonstrated to be an effective tool to control grain size and eventually the stress. Tensile stress is observed to increase substantially as a result of annealing up to 200 °C, which is suggested to be the result of elimination of voids.



## I. INTRODUCTION

Nanocrystalline materials demonstrate plastic and elastic properties essentially different from those of bulk materials.<sup>1,2</sup> For instance, intrinsic stresses in nanocrystalline films are extremely high, usually of the order of a GPa, i.e. well above the bulk yield strength. Despite considerable recent progress in understanding the stress development in thin nanocrystalline films, a thorough understanding of the stress buildup processes is not yet achieved.

Metallic multilayers are in particular suitable to investigate mechanical properties of nanocrystalline materials, especially with regard to grain size and interface effects, since these parameters can be conveniently controlled.<sup>3-9</sup>

In this chapter we address the relation between morphological features of nanocrystalline multilayered materials and their mechanical properties. Fe/Cu multilayers are used as a model system. The multilayers used are designed to investigate the effect of iron grain morphology on the state of stress. The Fe grain size is influenced by the presence of thin copper interlayers in between the Fe layers. It will be shown that besides grain size other morphological features such as the presence of voids are crucial for the mechanical behavior of nanocrystalline metals.

## II. EXPERIMENTAL METHODS

Fe/Cu multilayers are prepared in a Leybold Z550 magnetron sputtering system. The base pressure in this system is below  $7 \cdot 10^{-5}$  Pa and a working Ar-pressure of 4.8 Pa is used for deposition. Thermally oxidized 2-inch single crystalline Si-wafers with (100) orientation, used as substrates, are fixed on a rotating sample holder. The deposition is carried out at room temperature. The deposition rates are calibrated by thickness measurements applying weighing before and after the deposition of pure Fe (or Cu) layers and assuming bulk iron (or copper) density. The deposition rates are 3.1 nm/min for Fe and 5 nm/min for Cu. The Fe sub-layer thickness is varied from 13 nm to 54 nm; the copper interlayer thickness is taken 5 nm for all types of samples except one. Totally 5 types of multilayers are produced and investigated. The parameters are given in Table I.

TABLE I. Parameters of the investigated Fe-Cu multilayers.

Sample	Multilayer stacking	Total thickness (nm)
1	(5 nm Cu + 13 nm Fe) x 16	293
2	(5 nm Cu + 22 nm Fe) x 12	329
3	(5 nm Cu + 39 nm Fe) x 7	313
4	(5 nm Cu + 54 nm Fe) x 5	300
5	(20 nm Cu + 34 nm Fe) x 6	344

Thermal cycling experiments are performed inside the wafer curvature set-up (FSM 900TCvac system) in two consecutive steps: first up to 100 °C (150 °C for sample 2) and then up to 200 °C, where annealing is sustained for 5 min. The heating/cooling rate is below 2 °C/min. Before and after each annealing run X-ray diffraction (XRD) is applied at room temperature to monitor the stress changes in Fe layers.

The diffraction measurements are carried out using a Bruker-Nonius D5005 diffractometer equipped with a curved graphite monochromator in the diffracted beam, yielding Co  $K_{\alpha}$ -radiation. Stresses in Fe sublayers are determined applying the conventional  $\sin^2\psi$  stress analysis in  $\omega$ -geometry<sup>10</sup> using the {211} and {220} Fe diffraction lines. Tilt angles range from 2° to 40°. The X-ray elastic constants calculated according to Kröner-Eshelby<sup>10</sup> are applied.

Scanning electron microscopy (SEM) using a JEOL JSM-6500F is applied to analyze the surfaces of the films. On the basis of that the in-plane grain size is estimated. The microstructures of films on cross-sections are examined by a PHILIPS CM30T transmission electron microscope (TEM) operating at 300 kV. The samples are thinned to electron transparency by a Gatan PIPS 691 ion mill, using Ar ions.

### III. RESULTS

TEM and SEM images show that the multilayers consist of columnar grains (Fig. 1); the widths of the columns are almost constant from the substrate to the top. The in-plane grain size increases with iron sub-layer thickness (Fig. 2). It is remarkable that within a column the crystallite orientation of Fe is preserved through the 5 nm layers of copper (see Fig. 1), which is not observed for the sample No. 5, with 20 nm Cu layers. Bright-field TEM

images suggest the presence of very narrow, of the order of a nanometer, vertical crack-like voids along some grain boundaries (Fig. 3). After annealing up to 200 °C no morphological changes, e.g. grain size or shape, surface or interface roughness, could be observed with electron microscopy. Voids are present both before and after annealing for all samples.

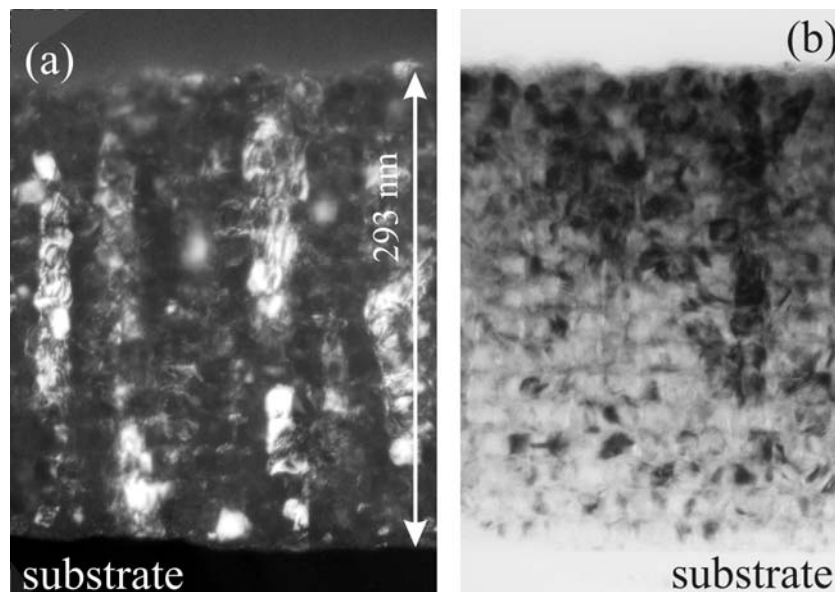


Fig.1. (a) Dark-field (of  $\{110\}$  bcc Fe reflection) and (b) bright-field TEM images of the multilayer No. 1. Columns have thickness independent on distance from the substrate. Iron sub-grains preserve their orientation through Cu-layers (not visible in bright-field mode).

XRD pole figures measured for  $\{110\}$  and  $\{211\}$  bcc Fe peaks show a weak fiber  $\langle 111 \rangle$ -texture: the difference between the strongest and the weakest intensity is not more than a factor 2.

Both the X-ray (Fig. 4) and selected area electron diffraction patterns of multilayers with 5 nm copper interlayer show very weak diffraction peaks of fcc Cu. In contrast, for the sample with 20 nm copper interlayer the intensities pertaining to fcc Cu diffraction peaks are much more pronounced than expected on the basis of the layer thickness with respect to that of the multilayers with 5 nm copper interlayers (Fig. 4). No changes in peak intensities are observed after annealing up to 200 °C for all samples.

XRD and wafer curvature measurements show that the stresses in the multilayers are biaxial and rotationally symmetric. All stress values mentioned in this chapter refer to stresses in the plane of the film. In all films high tensile stresses (0.5 GPa – 1.0 GPa) are observed by XRD and wafer curvature technique. The stresses depend on Fe sub-layer

thickness and seem independent of Cu-content (Fig. 2, compare data for 5 nm and 20 nm Cu interlayers). The higher stress values are found for thicker iron sub-layers.

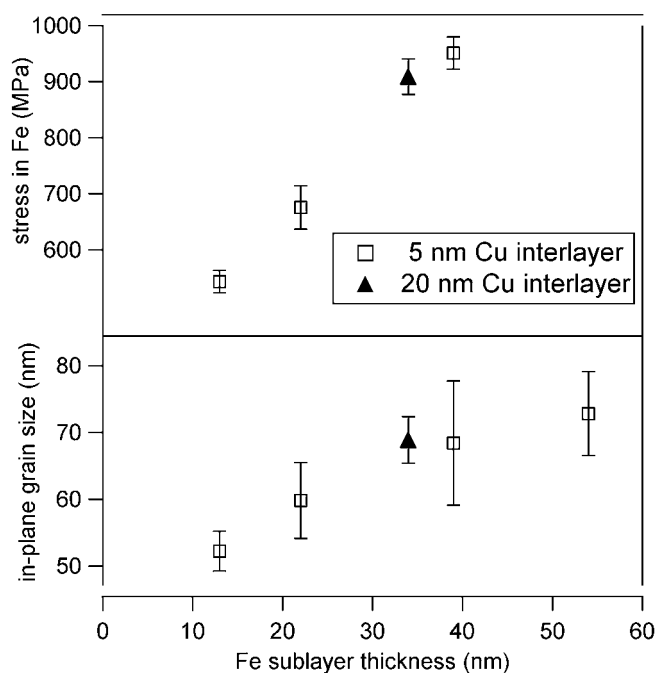


Fig.2. In-plane grain size as a function of Fe sublayer thickness and in-plane stress in Fe as measured by XRD at room temperature for as-deposited films. The stress depends on Fe layer thickness or grain size rather than on Cu-content.

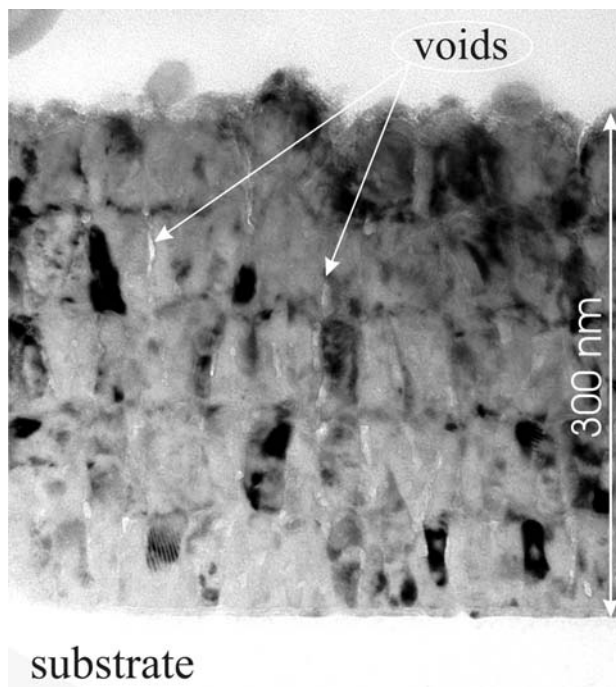


Fig.3. Defocused bright-field TEM image of a multilayer. Vertical nano-voids along some grain boundaries are outlined by Fresnel-fringes.

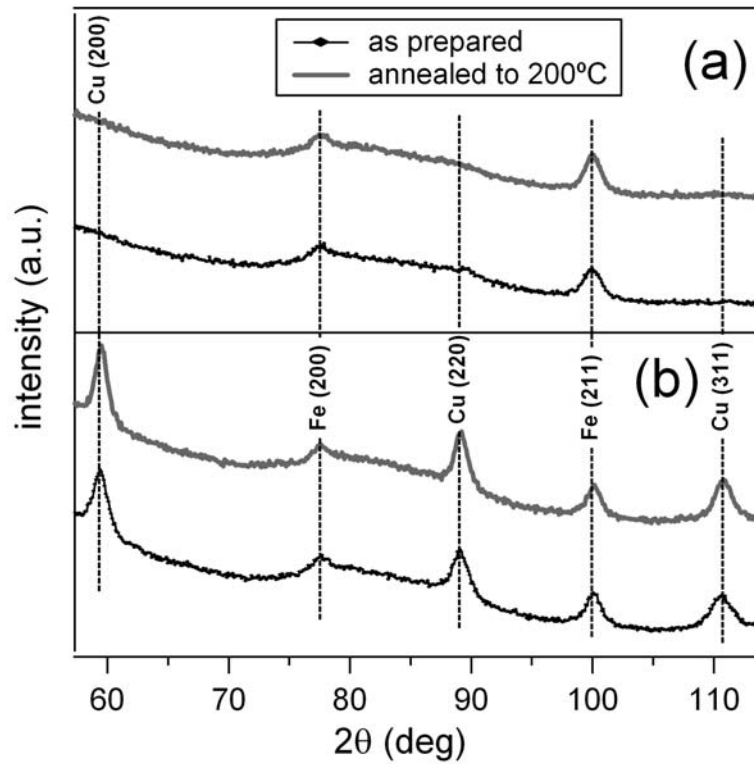


Fig.4. X-ray diffraction patterns of the multilayers with (a) 5 nm copper interlayers (Sample No.1) and (b) 20 nm Cu interlayers (No.5), as deposited and after annealing. The spectra are shifted vertically for comparison. The scale is the same for all spectra.

As a result of annealing the stresses in the Fe phase as measured by XRD  $\sin^2\psi$ -method in all samples are found to increase (Fig. 5). The increase in stress is larger for the finer multilayers (these are also the films with lower initial stress). Annealing up to 200 °C leads to stress increases by up to 200 MPa.

#### IV. DISCUSSION

The lack of pronounced diffraction peaks of fcc Cu in both X-ray (Fig. 4) and electron diffraction patterns of specimens with 5 nm Cu interlayers in contrast to the very prominent fcc Cu peaks for the specimen with 20 nm Cu interlayers is remarkable. The effect of small grain size cannot lead to this, as estimates of a ‘size effect’ on the X-ray diffraction peak broadening according to the Scherrer formula (the approach described in Ref. 11 is used) yield broadening about 2-3 deg, which peaks should still be clearly visible. The other possible explanations of the absence of clear diffraction lines of fcc Cu in specimens with 5 nm copper

interlayers are (i) the formation of a Cu-Fe bcc solid solution or the formation of copper in either (ii) an amorphous or (iii) a bcc phase.

According to the Cu-Fe phase diagram a maximum of  $1.88 \pm 0.5$  at.% of Cu can be dissolved in bcc Fe at  $850^\circ\text{C}$ ,<sup>12</sup> so it is not very likely that a metastable solution of as much as 30 at.% of Cu in bcc Fe forms (implying that all Cu dissolves in Fe homogeneously).

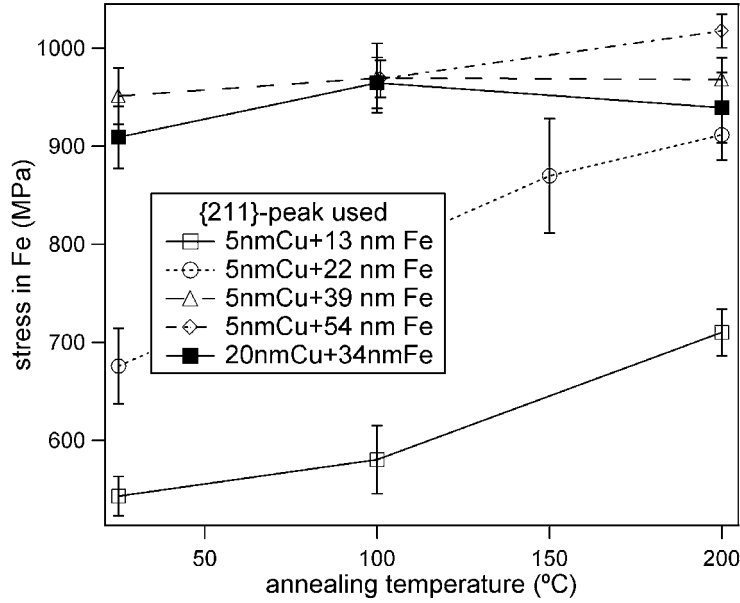


Fig.5. In-plane stress in Fe (measured by XRD at room temperature) as a result of annealing.

Amorphous Cu in Fe-Cu system was not reported so far (see discussion in Ref. 13). On the other hand, the growth of bcc copper on Fe substrates was previously experimentally observed.<sup>14,15</sup> Tang and co-workers described bcc Cu using *ab initio* calculations,<sup>16</sup> showing that the lattice mismatch between bcc Cu and bcc Fe is very small ( $\sim 1.4\%$ ) as compared to the misfit between fcc Cu and bcc Fe. The low lattice mismatch reduces the (elastic) energy per unit interface, making it energetically favorable for the two bcc phases to grow epitaxially on one another. Our observation, that the crystallographic orientation of iron is preserved even when a 5 nm layer of Cu is present (Fig. 1), points to such epitaxial growth.

As described in Section III, the grains in sputtered Fe/Cu multilayers do not have the tapered grain structure often found in metal thin films. For instance, the pure Fe thin films, deposited using exactly the same deposition conditions as in the present study, have shown a considerable in-plane grain size increase with film thickness (see Chapter IV of this thesis

and Ref. 17). However, if a 5 nm Cu interlayer interrupts the Fe layer, the columnar width is nearly constant (Fig. 1).

The tapered columnar grain structure in thin films is usually described in terms of a so-called ‘evolutionary selection’,<sup>18</sup> i.e. some grains are energetically or kinetically favored (preferred crystallite orientation or larger size, overshadowing neighbors) over neighboring grains. Such grains outgrow their neighbors. However, a thin layer of a metal with higher surface atom mobility (such as Cu, as here is the case) can reduce the advantage of one column over another by altering the texture of the next layer (if growth is not epitaxial) and by smoothening the surface. The observed preservation of crystallite orientation of iron through copper interlayers suggests that the latter mechanism, i.e. smoothening of the interface by reducing shadowing effects, plays the most important role in preventing lateral growth of Fe grains.

The comparison with the pure Fe films, deposited using the same conditions, can be continued with regard to the mechanical behavior. The state of stress versus grain size in as-deposited Fe-Cu multilayers is essentially different from that of the pure Fe films (see Chapter IV of this thesis and Ref. 17) (Fig. 6). The stress increases with increasing grain size in pure Fe films, whereas the multilayers exhibit quite the opposite behavior. This comparison demonstrates that grain size (or density of grain boundaries) is not the only parameter that controls the stress under fixed deposition conditions, as was suggested in the early 70-s by Doljack and Hoffman.<sup>19</sup> Obviously, other morphological features like the presence and geometry of voids, grain shape as well as interface phenomena can play an important role.

The tensile stress occurrence and evolution in the multilayers will be discussed in terms of (i) grain shape, (ii) the influence of interface roughness, (iii) the effect of Fe/Cu intermixing at interfaces, and (iv) coalescence-driven stress buildup.

As a result of the columnar grain shape (in comparison to the tapered grains of pure Fe films) the in-plane grain size distribution of the Fe-Cu multilayers is expected to be narrower than in the pure Fe films. However, the tensile stress behavior of the multilayers is qualitatively different from that of the iron films (Fig. 6), i.e. for smaller grains in multilayers lower stress is observed, while the opposite holds for the iron films. Another possible effect of grain shape is that practically all grain boundaries of tapered grains are not normal to the direction of stress. This can lead to a stress relief by the grain boundary sliding mechanism.<sup>20</sup>

In that case a tapered grain structure would demonstrate lower stress than a perfectly columnar one, which is opposite to the observations shown in Fig. 6.

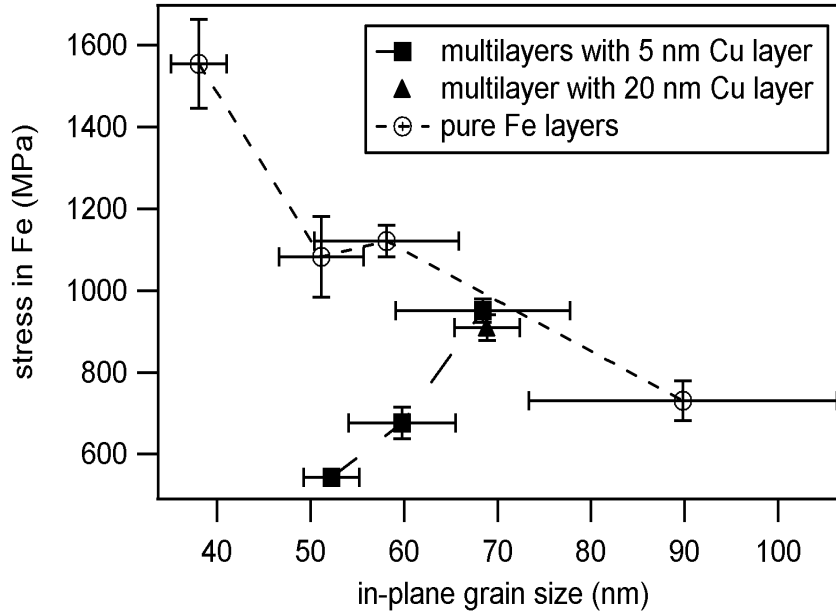


Fig.6. In-plane stress in iron (measured by XRD at room temperature) for as-deposited pure Fe films (from [17]) and Fe/Cu multilayers.

That interface roughness can affect stress states of thin films was shown in Ref. 21: the multilayered structure in W thin films dramatically reduces stress level. The explanation generally put forward is that an the increased (interface) roughness diminishes the stress buildup in the next layer during deposition simply by delaying the onset of a stress buildup until roughness becomes small as compared to growing layer thickness. The roughness of the Fe/Cu interface may account for the substantial differences between stresses in Fe/Cu multilayers and those in pure Fe films. However, roughness changes cannot explain the stress increase in multilayers as a result of annealing, because roughness does not act as a stress buildup mechanism itself.

Interdiffusion of copper or other atoms into the Fe lattice can cause considerable hydrostatic equilibrium volume changes thereby altering stress states. Such hydrostatic equilibrium volume changes can be monitored through the XRD stress measurement, as for a biaxial stress state the stress-free lattice spacing can be extracted from  $\sin^2\psi$  data.<sup>10</sup> The shrinkage of the stress-free lattice spacing upon annealing would lead to a tensile stress increase. However, the experimentally observed behavior of the stress-free lattice spacing of Fe is opposite (Fig. 7), an increase of stress-free lattice volume with annealing is found.



Furthermore, the increase of stress-free lattice spacing with annealing does not correlate with the stress increase. For example, the lattice spacing increases considerably for samples 4 and 5, while the stress increase is very weak or absent in these multilayers. These observations suggest that the observed tensile stress increase upon annealing could not be explained by interdiffusion.

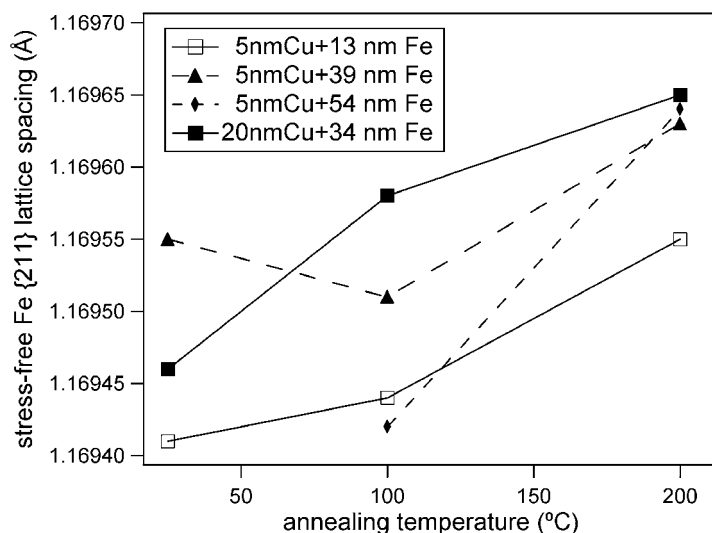


Fig.7. Stress-free Fe {211} lattice spacing as determined from XRD room temperature  $\sin^2 \psi$ -measurements.

The grain coalescence mechanism is another possible explanation for the observed tensile stress increase. This mechanism is responsible for a tensile stress buildup during growth of thin nanocrystalline films.<sup>22-25</sup> The driving force behind the process is an energy gain from voids' closure, e.g. free surfaces are eliminated and a grain boundary is formed instead. As revealed clearly by electron microscopy analysis such nano-voids are present along some grain boundaries in the studied multilayers. Thus the multilayers are potentially able to release energy and increase the tensile stress by the coalescence process.

According to the coalescence model (see Refs. 22, 25 and Chapter III of this thesis), grains have to stretch elastically, i.e. overcome a barrier, before a gap between two grains closes. The high temperature treatment may facilitate the coalescence process by relaxing stress during annealing (due to thermal expansion coefficients' mismatch between metal film and silicon substrate). Lower stress at higher temperature reduces the energy barriers and coalescence becomes more effective, leading to a tensile stress increase upon annealing.

## V. CONCLUSIONS

The tensile stress increases significantly in Fe-Cu multilayers as a result of annealing up to 200 °C. This phenomenon is explained by grain coalescence process: due to a stress reduction at elevated temperatures, it becomes easier for neighboring grains to close nano-voids, leading to an overall stress increase.

The results of this investigation show that grain size is not the only parameter that controls the intrinsic stress state in thin films. The presence of voids also plays an important role.

The results also indicate that bcc copper forms in sputtered Fe-Cu multilayers for Cu layer thickness of 5 nm and Fe volume fraction more than 70%.

It is demonstrated that an interlayer can be effective to control grain size and eventually stress in thin metallic films.

## REFERENCES

- 1 S.C. Tjong, H. Chen, Materials Science and Engineering R **45**, 1 (2004).
- 2 K.S. Kumar, H. Van Swygenhoven, S. Suresh, Acta Mater **51**, 5743 (2003).
- 3 F. Martin, C. Jaouen, J. Pacaud, G. Abadias, Phys Rev B **71**, 045422 (2005).
- 4 M. Jaouen, J. Pacaud, C. Jaouen, Phys Rev B **64**, 144106 (2001).
- 5 A.C. Lewis, D. Josell, T.P. Weihs, Scripta Mater **48**, 1079 (2003).
- 6 X.W. Zhou, H.N.G. Wadley, R.A. Johnson, D.J. Larson, N. Tabat, A. Cerezo, A.K. Petford-Long, G.D.W. Smith, P.H. Clifton, R.L. Martens, T.F. Kelly, Acta Mater **49**, 4005 (2001).
- 7 A. Misra, M. Verdier, Y.C. Lu, H. Kung, T.E. Mitchell, M. Nastasi, J.D. Embury, Scripta Mater **39**, 555 (1998).
- 8 N. Mara, A. Sergueeva, A. Misra, A.K. Mukherjee, Scripta Mater **50**, 803 (2005).
- 9 S. Labat, F. Bocquet, B. Gilles, O. Thomas, Scripta Mater **50**, 717 (2004).
- 10 V.M. Hauk, and E. Macherauch, Adv. in X-ray Anal. **27**, 81 (1983).
- 11 R. Delhez, T.H. de Keijser, J.I. Langford, D. Louër, E.J. Mittemeijer, and E.J. Sonneveld: *The Rietveld Method*, edited by R.A. Young, Oxford University Press, New York, NY, 1993, pp. 132-66.
- 12 T.B. Massalski, et al (editors). *Binary Alloy Phase Diagrams*, 2nd edition. ASM International, 1990, p. 1408.
- 13 Z.F. Li, W.S. Lai, B.X. Liu, Appl Phys Lett **77**, 3920 (2001).
- 14 Z.Q. Wang, S.H. Lu, Y.S. Li, F. Jona, P.M. Marcus, Phys Rev B **35**, 9322 (1987).
- 15 B. Heinrich, Z. Celinski, J.F. Cochran, W.B. Muir, J. Rudd, Q.M. Zhong, A.S. Arrott, K. Myrtle, J. Kirschner, Phys Rev Lett **64**, 673 (1990).
- 16 Z. Tang, M. Hasegawa, Y. Nagai, M. Saito, Phys Rev B **65**, 195108 (2002).
- 17 N.R. Shamsutdinov, A.J. Böttger, R. Delhez, N.M. van der Pers, F.D. Tichelaar, Metallurgical and Materials Transaction A (submitted).
- 18 A. Van der Drift, Philips Res Repts **22**, 267 (1967).

- 19 F.A. Doljack, R.W. Hoffman, *Thin Solid Films* **12**, 71 (1972).
- 20 C. Zener, *Phys. Rev.* **60**, 906 (1941).
- 21 T. Karabacak, C.R. Picu, J.J. Senkevich, G-C. Wang, T-M. Lu, *J Appl Phys* **96**, 5740 (2004).
- 22 W.D. Nix, B.M. Clemens, *J Mater Res* **14**, 3467 (1999).
- 23 S.C. Seel, C.V. Thompson, S.J. Hearne, J.A. Floro, *J Appl Phys* **88**, 7079 (2000).
- 24 L.B. Freund, S. Suresh, *Thin Film Materials. Stress, Defect Formation and Surface Evolution* (Cambridge University Press, Cambridge 2003), p.70.
- 25 N.R. Shamsutdinov, A.J. Böttger, *Acta Mater* (submitted).

## SUMMARY

Nanocrystalline metals play a crucial role in developing technologies. Their mechanical properties and stability strongly depend on morphological features such as grain size and shape, presence and geometry of voids, texture, etc. Such phenomena as anomalous elasticity and plasticity in these materials are not yet fully understood due to lack of a consistent experimental effort that addresses the effects of morphological features. This thesis represents a study that combines several experimental techniques such as X-ray diffraction, electron microscopy, photoelectron spectroscopy and wafer curvature to investigate the relation between mechanical properties of nanocrystalline metals (with emphasis on 3d transition series) and their morphology.

A method is developed that allows experimental determination of surface properties of a crystalline 3d transition metal (Chapter II). The method employs the equivalent core approximation that relates surface segregation energies to differences in positions of core-level photoelectron peaks that correspond to surface and bulk atoms. The main obstacle to overcome is the sufficiently accurate determination of the positions of two overlapping peaks of complex shape. By gathering data in such a way, that the surface sensitiveness of photoelectron spectroscopy alters, the relative intensity of the two peaks is changed. Then a specially developed fitting routine is applied to extract the surface-bulk peak position difference. The method is tested on the example of Cu and showed agreement with the available *ab initio* estimates.

A model to account for anomalous elasticity in nanocrystalline films is developed (Chapter III) using the grain coalescence model, which is based on balancing the grain boundary/surface energy with elastic energy. If voids are present and narrow enough then it might be energetically favorable to stretch the material and close the voids. The original grain coalescence model by Nix and Clemens was developed to explain the intrinsic tensile stress in thin polycrystalline films employing simple energetic considerations: when the energy gain from substituting two side surfaces of two neighboring grains by a grain boundary overweighs the elastic energy required to stretch the grains to reach each other, then the grains coalesce, giving rise to intrinsic tensile stress. In the present thesis this model is

expanded to describe a wider class of nanocrystalline materials. Instead of considering a particular grain shape, the distribution of voids is introduced as a more general description of film morphology, and a relation between tensile stress and morphology of nanocrystalline film is obtained. Moreover, the model presented in this thesis goes a step further and accounts also for elastic properties of nanocrystalline materials. The experimental part of the study on magnetron sputtered nanocrystalline Fe thin films demonstrated a good agreement of the model predictions for *both* stress *and* elasticity.

The last two chapters of this thesis are dedicated to the experimental analysis of the relation between mechanical properties and morphological features of nanocrystalline thin films (Fe) and multilayers (Fe-Cu). The films are deposited using magnetron sputtering. Transmission and scanning electron microscopy are applied to monitor changes in morphology, while X-ray diffraction and wafer curvature methods are used to investigate stress states and elastic properties, crystal structure and texture. A method is developed to determine orientation distributions of dislocations from X-ray diffraction line profile analysis. First, the X-ray diffraction line broadening is modeled for certain dislocation arrangements. Then a combination of the modeled diffraction line broadenings is fitted to a set of measured X-ray diffraction line widths. The resulting orientation distribution of dislocation densities provides a valuable illustration of the mechanical processes in the material. For the case of Fe thin films it is shown that annealing can lead to annihilation of dislocations with the glide direction along the maximum resolved shear stress. The dislocations with glide direction along the maximum resolved shear stress tend to disappear as a result of annealing up to 400 °C. However, the initially high tensile stresses in films (of the order of 0.5-1 GPa) are observed to *increase* upon annealing. This stress increase obviously cannot be explained by dislocation-mediated plastic relief. So simultaneously with the dislocation movement there is another processes occurring that is associated with nano-voids elimination at grain boundaries, which leads to a complex mechanical response of nanocrystalline films.

In Chapter V the experimental study of Fe/Cu multilayers shows that remarkably different stress states as compared to pure Fe films are present. The stresses in multilayers are considerably weaker (between 0.5 GPa and 0.9 GPa as compared to those of 0.7 to 1.6 GPa in pure Fe films). Further, a significantly stronger tensile stress increase upon annealing in multilayers is observed than for the case of pure Fe films. These findings clearly demonstrate the importance of grain coalescence mechanism, which is expected to be especially

pronounced in sputtered materials, as they often demonstrate a relatively open micro-structure, i.e. presence of voids along some grain boundaries.

## SAMENVATTING

Nanokristallijne materialen spelen een belangrijke rol in de huidige technologische ontwikkelingen. Daarbij zijn mechanische eigenschappen en stabiliteit van nanokristallijne materialen doorslaggevend voor verdere toepassingen. Zowel het mechanisch gedrag als de stabiliteit hangen sterk af van de microstructuur en de morfologie van het materiaal, met name voor wat betreft korrelgrootte en -vorm, aanwezigheid en geometrie van holtes, en textuur. Een behoorlijk aantal verschijnselen, zoals anomale elasticiteit en plasticiteit, zijn niet goed begrepen, met name omdat systematisch onderzoek naar de invloed van de microstructuur op deze eigenschappen ontbreekt. Dit proefschrift omvat een studie waarbij zowel het mechanisch gedrag als de microstructuur van nanokristallijne metalen (in het bijzonder 3d overgangsmetalen) is onderzocht, gebruik makend van verschillende experimentele technieken, waaronder röntgendiffractie, elektronenmicroscopie, foto-elektronspectroscopie en substraatkrummingsmetingen.

Daarnaast is een methode ontwikkeld waarmee oppervlakte-eigenschappen van kristallijne 3d overgangsmetalen bepaald kunnen worden (Hoofdstuk II). De methode maakt gebruik van de zogenaamde ‘equivalente kern’ benadering. Deze benadering relateert oppervlakte-segregatie-energie aan verschillen in de energie van foto-elektronen afkomstig van oppervlakte-atomen en die van foto-elektronen afkomstig van atomen binnenin het materiaal. Door meetgegevens op een dusdanige manier te verzamelen dat de oppervlaktegevoeligheid verandert, kunnen de relatieve bijdragen van de twee pieken gevarieerd worden. Om de posities (energieën) van de twee overlappende pieken – met ingewikkelde piekvorm – met voldoende nauwkeurigheid te bepalen, is een speciale fit-routine ontwikkeld. De methode is getest op Cu en de gevonden waarden voor de segregatie-energie komen overeen met resultaten van ab initio berekeningen.

Een model dat het anomale elastisch gedrag van nanokristallijne laagjes kan verklaren is beschreven in Hoofdstuk III. Daarbij wordt gebruik gemaakt van een coalescentiemodel van de korrels dat is gebaseerd op een energiebalans tussen korrelgrens en oppervlakte-energie enerzijds en elastische energie anderzijds. In aanwezigheid van voldoende kleine holtes kan het energetisch voordeliger zijn voor het rondom een holte liggende materiaal om



te expanderen en daarmee de holte te sluiten. Het originele model voor coalescentie van korrels, van Nix en Clemens, was in staat om de intrinsieke trekspanning in dunne polykristallijne films te verklaren op basis van de volgende redenering: als de te boeken energiewinst door het vervangen van de beide (vrije) oppervlakken van naburige korrels door een korrelgrens groter is dan de elastische energie nodig voor het expanderen van het korrelmateriaal, dan treedt coalescentie van korrels op, hetgeen gepaard gaat met het ontstaan van een intrinsieke trekspanning. Dit model is in dit proefschrift uitgebreid zodat een breder scala aan nanokristallijn materiaal beschreven kan worden. Zo is, in plaats van een specifieke korrelvorm, een verdeling van holtes geïntroduceerd als een meer algemene beschrijving van de microstructuur van dunne lagen; hiermee is dan een relatie tussen trekspanning en microstructuur van de nanokristallijne films gelegd. Het in dit proefschrift ontwikkelde model gaat echter een stap verder, omdat het ook elastische eigenschappen van nanokristallijn materiaal kan verklaren. Experimenten aan nanokristallijne ijzerlagen tonen aan dat het model zowel de spanning als het elastisch gedrag goed kan voorspellen.

De laatste twee hoofdstukken van dit proefschrift betreffen de analyse van de relatie tussen mechanische eigenschappen en microstructuur van nanokristallijne dunne films (Fe) en multilagen (Fe/Cu). De veranderingen in microstructuur na warmtebehandelingen zijn met behulp van transmissie- en rasterelektronen-microscopie gevolgd. De kristalstructuur, textuur, spanningstoestand en elastische eigenschappen zijn via röntgendiffractie en substraatkrommingsmetingen bepaald. Om de bijdrage van dislocaties te onderzoeken is een methode ontwikkeld om de oriëntatieverdeling van dislocaties te bepalen op basis van röntgendiffractie-lijnprofielanalyse. Eerst is een model opgesteld dat de lijnverbreding beschrijft die optreedt bij welbepaalde dislocatieverdelingen. Daarna werd een combinatie van gemodelleerde diffractielijnverbredingen gefit aan een serie gemeten lijnbreedtes. De resulterende oriëntatieverdeling van dislocaties verschaft inzicht in de mechanische processen in het materiaal. In het geval van dunne ijzerfilms is aangetoond dat warmtebehandelingen op 400 °C kunnen leiden tot het annihileren van dislocaties met glijrichting langs de maximale schuifspanning. Alhoewel sommige dislocaties verdwijnen, nemen de initiële hoge trekspanningen in de films (van de orde 0.5–1 GPa) desondanks toe na warmtebehandeling. De spanningstoename kan uiteraard niet begrepen worden op basis plasticiteit (relaxatie) door dislocatiebeweging. Dit leidt tot de conclusie dat een ander proces optreedt, namelijk een dat gerelateerd is aan het verdwijnen van nanoholtes aan korrelgrenzen (coalescentie van

korrels). De combinatie van beide processen leidt tot de waargenomen complexe mechanische respons van nanokristallijne films.

In Hoofdstuk IV toont experimenteel onderzoek aan Fe/Cu multilagen aan dat de multilagen in vergelijking tot enkelvoudige Fe films een opvallend andere spanningstoestand hebben. De spanningen in de multilagen zijn duidelijk lager i.e. tussen 0.5 GPa en 0.9 GPa, te vergelijken met 0.7 tot 1.6 GPa in Fe films. Verder vertonen de multilagen een significant hogere toename in trekspanning na veroudering dan de Fe lagen. De waarnemingen tonen het belang van het mechanisme van korrelcoalescentie duidelijk aan. Dit mechanisme is met name te verwachten in magnetrongesputterde lagen, omdat daarin veelal een relatief open microstructuur, met name de aanwezigheid van holtes aan korrelgrenzen, waargenomen wordt.

## **ACKNOWLEDGEMENTS**

I am very grateful to all those who taught me about natural sciences, but special thanks to my schoolteacher Gennadij Rjazanov. Thanks to my colleagues at Frank Laboratory of Neutron Scattering, Fraunhofer Institute for Non-Destructive Testing and Delft University of Technology. Thanks to those who read (parts of) the manuscript and gave me extensive comments. Thanks to Amarante Böttger who guided me through the project. I am extremely grateful to all my friends. Special thanks to my parents who invested in my education everything they could. Finally, thanks to Natalia for her love and support.

## Curriculum Vitae

Nail Shamsutdinov

Date of birth: 16<sup>th</sup> of May, 1973

Education:

1990 – 1996: Diploma of Engineer-physicist. Department of Solid State Physics, Faculty of Experimental and Theoretical Physics at Moscow Engineering-Physics Institute (State University).

Research Work:

1996 – 2001: Junior Researcher at Frank Laboratory of Neutron Scattering, Joint Institute for Nuclear Research (Dubna, Russia).

2001 – 2005: PhD researcher at Delft University of Technology, Department of Materials Science and Technology.